UNIVERSITY OF CALIFORNIA

Los Angeles

Training Issues in High-Speed Fiber-Optic and Radio Communication Systems

A dissertation submitted in partial satisfaction

of the requirements for the degree

Doctor of Philosophy in Electrical Engineering

by

Hong Chen

2003

The dissertation of Hong Chen is approved.

_____

Mario Gerla

_____

Ming Wu

_____

Babak Daneshrad

_____

Gregory J. Pottie, Committee Chair

University of California, Los Angeles

2003

To my parents and my sister

TABLE OF CONTENTS

List of Figures

LIST OF TABLES

ACKNOWLEDGMENTS

My greatest gratitude goes to my advisor Professor Greg Pottie. Greg has been instrumental in ensuring my academic, professional, and financial well being. In every sense, none of this work would have been possible without his support.

I sincerely thank Professor Babak Daneshrad, Professor Maris Gerla, and Professor Ming Wu, for taking time to serve on my dissertation committee and provide me with valuable input.

My great appreciation also goes to Professor Stephen E. Jacobsen, for being my initial advisor, and to Professor Ali H. Sayed, for guiding me during my beginning years at UCLA.

I am very grateful to my industry mentors who generously shared their time, in-depth knowledge, and expertise with me when I was working with them during the summer. They are Dr. Nick Frigo of ATT Labs-Research, Dr. Ke Han of Marvell (was with Quantum), Dr. Bob Jopson and Dr. Herwig Kogelnik of Bell-Labs, Dr. Cedric Lam of Opvista (was with ATT Labs-Research), and Dr. Peter McEwen (was with Quantum and passed away in November 2001). I am also indebted to Dr. Jerry Foschini who led me to the area of polarization mode dispersion.

Many many thanks also go to my dear friends at UCLA and those in the Bay area for their friendship, hospitality, and kind advice.

My final heartfelt acknowledgment goes to my husband Chengang. His support and encouragement has turned my journey through Ph.D. studies into a pleasure. He has my everlasting love.

Vita

1970	Born, Anhui, People's Republic of China.
1989	B.E. (Computer Science), Hefei University of Technology, Hefei, Anhui, China.
1992	M.E. (Automatic Control), University of Science and Technology of China (USTC), Hefei, Anhui, China.
1992–1997	Researcher and Lecturer, Automatic Control Department, USTC, Hefei, Anhui, China.
1998–1999	Grader, Electrical Engineering Department, UCLA.
1999–2001	Teaching Associate, Electrical Engineering Department, UCLA.
2001–2003	Research Assistant, Electrical Engineering Department, UCLA.

Publications

1. Hong Chen and Gregory J. Pottie, An Orthogonal Projection-Based Approach for PAR Reduction in OFDM, IEEE Communications Letters, vol. 6, pp. 169-71, May 2002.

2. H. Chen, C. F. Lam, N. J. Frigo, G. J. Pottie, P. D. Magill, and M. Boroditsky, A One-Input Two-Output Channel Representation for Single-Mode Fibers with PMD, Journal of Lightwave Technology, vol. 21, pp. 743-9, Mar. 2003.

3. Hong Chen, Robert M. Jopson, and Herwig Kogelnik, On the Bandwidth of Higher-Order Polarization-Mode Dispersion: the Taylor Series Expansion, Optics Express, vol. 11, pp. 1270-82, Jun. 2003.

4. Hong Chen and Greg Pottie, A Comparison of Frequency Offset Tracking Algorithms for OFDM, WC27-4, Globecom 2003.

5. Ali H. Sayed and Hong Chen, A Uniqueness Result Concerning a Robust Regularized Least-Squares Solution, Systems Control Letters, vol. 46, pp. 361-9, Aug. 2002.

ABSTRACT OF THE DISSERTATION

Training Issues in High-Speed Fiber-Optic and Radio Communication Systems

by

Hong Chen

Doctor of Philosophy in Electrical Engineering

University of California, Los Angeles, 2003

Professor Gregory J. Pottie, Chair

Training is an integral phase of information transmission over a wired or wireless channel. During the training period, channel estimation, frequency synchronization, and timing recovery are conducted for enabling a reliable information bit recovery at the receiver.

This thesis proposes and verifies in simulation several new ideas and methods that facilitate the training process, optimize the performance of parameter estimation, and maintain a delicate balance between training and data transmission. The goal is to achieve energy-efficient communications over time-varying frequency-selective fiber optic links and radio channels.

Its contributions towards combating dispersive fiber optic channels include a novel description of polarization mode dispersion effects in single-mode fibers, allowing the traditional training and equalization techniques to be applied in compensating the polarization mode dispersion, and an original training-based approach that compensates the first-order polarization mode dispersion at low cost.

For radio communications, this thesis addresses three important design issues

in utilizing the orthogonal frequency division multiplexing (OFDM) technique. OFDM has gained increasing interest, due to its high spectral efficiency and robustness against multipath fading. The main disadvantages of OFDM are its low power efficiency caused by the high peak-to-average power ratio of OFDM signals, and its high sensitivity to frequency synchronization errors. Among our contributions are a fast algorithm that efficiently reduces the peak-to-average power ratio of OFDM signals at low overhead, an extensive comparison of frequency offset tracking algorithms, and finally, closed-form expressions of optimal training length that enables fast training length adjustment to maximize system throughput under varying channel conditions.

CHAPTER 1

Introduction

Training is an integral phase of information transmission over a wired or wireless channel. During the training period, channel estimation, frequency synchronization, and timing recovery are conducted for enabling the information bit detection at the receiver. This thesis proposes and verifies in simulation several new ideas and methods that facilitate the training process, optimize the performance of parameter estimation, and maintain a delicate balance between training and data transmission. The goal is to achieve energy-efficient communications over time-varying frequency-selective fiber optic links and radio channels.

This first chapter presents the motivation behind this thesis, and defines the fundamental problems considered. It also summarizes the contributions made toward these problems, and outlines the remaining chapters.

1.1 Motivation

1.1.1 Radio Communications and Fiber-Optic Transmissions

Recently, increasing research and development activities have been seen in two of the hottest areas of telecommunications: wireless communications and fiber-optic transmissions. Now being introduced into the global communications infrastructure at an astonishing pace, both wireless and optical technologies are

revolutionizing the industry and will undoubtedly dominate its future.

Wireless communications are driven by the desire for change from wired fixed place-to-place communications to wireless mobile person-to-person communications, and for the ability to share information around the world with anyone, anywhere, at any time. Wireless applications include cellular systems, wireless local area networks (LAN), home wireless networking, and audio/video broadcasting. Based on the target data rate, achievable transmission range, and constraint on the power use, wireless communication standards can be classified into four groups: (1) High power, wide area systems; (2) Low power, local area systems; (3) Low data rate, wide area systems; (4) High data rate, local area systems. To date, the achievable range of successful wireless transmissions is from 10 meters to several kilometers, and the realistic data rate through radio channels is up to 54 Mbit/s.

In the meanwhile, fiber optics has been utilized since the late 1970s to provide long-range high-speed transmission at low cost [1]. In 1977, fiber optic telephone systems were first installed in Chicago and Boston respectively. By the early 1980s, single-mode fiber operating in the 1310 nm and later the 1550 nm wavelength windows became the standard fiber installed for these networks. Today, computers, information networks, and data communications also embrace fiber optic transmission. Particularly, due to the successful development of dense wavelength-division multiplexing (DWDM) technology, fiber transmission capacity has grown by a factor of 100 in the last decade. In 1990, Bell Labs transmitted a 2.5 Gb/s signal over 7,500 km without regeneration. In 1998, Bell Labs researchers transmitted 100 simultaneous optical signals, each at a data rate of 10 Gbits/s for a distance of nearly 250 miles (400 km). This increased the total data rate on one fiber to one Tbits/s.

1.1.2 Challenges in Radio Communications and Fiber-Optic Transmissions

There are many technological challenges in both areas, due to channel impairments, bandwidth limitations, energy limitations, and delay constraints. The impairment described as time-varying linear dispersion is the focus of this thesis.
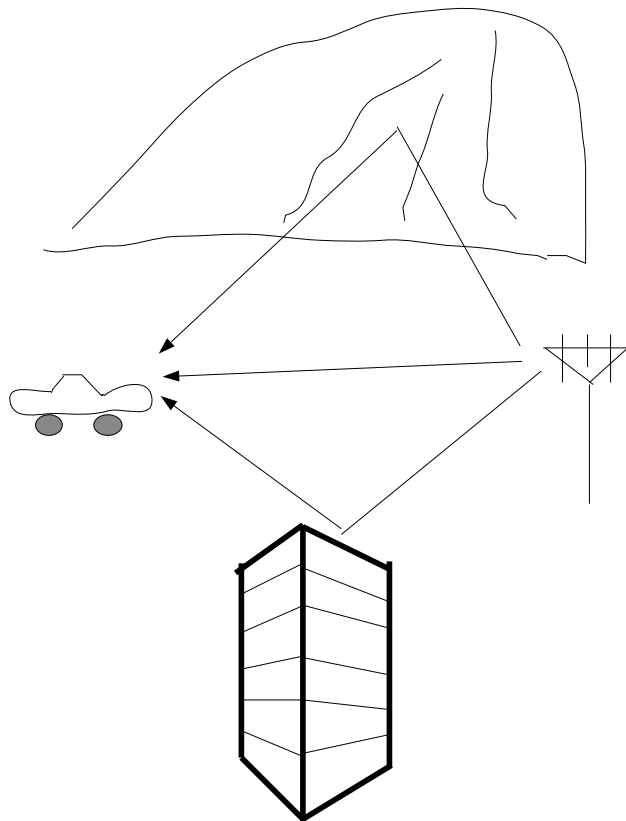
Figure 1.1: A typical multipath channel in wireless communications.

In a wireless scenario as shown in Fig. 1.1, the incoming radio waves ar-

rive from different directions with different propagation delays [49]. The signal received by the mobile at any point in space may consist of a large number of plane waves having randomly distributed amplitudes, phases, and angles of arrival. These multipath components combine vectorially at the receiver antenna, and can cause the signal received by the mobile to distort or fade. Even when a mobile receiver is stationary, the received signal may fade due to movement of surrounding objects in the radio channel. Multipath generates inter-symbol interference (ISI) in the received symbols and therefore poses significant challenges in the development of wireless systems.

To combat the multipath fading channels, a special multi-carrier modulation, namely orthogonal frequency division multiplexing (OFDM), has been proposed as an effective modulation scheme. It has recently been adopted as standard for high-speed wireless LANs, video/audio broadcasting, and 4G cellular systems. The major design issues in utilizing OFDM include reducing its high peak-to-average power ratio, which otherwise results in a low power efficiency, and minimizing its frequency synchronization errors. Several topics related to these two issues will be addressed in this thesis.

Dispersion is also a fundamental limit to the performance of data transmission over fiber optic links. In a single mode fiber, when light travels down toward the receiver, it has two orthogonal polarization modes that follow the path of two axes. When the core of the fiber is asymmetrical, as shown in Fig. 1.2 (b), the light travelling along one polarization axis moves slower than the light polarized along the other axis. This effect is known as the polarization mode dispersion (PMD). It broadens the pulse enough to make it overlap with other pulses or change its own shape enough to make it undetectable at the receiver. PMD is a challenging issue due to its statistical nature. Research directions in the

(a)

Vertical polarization

fiber

Horizontal polarization

(b)

Vertical polarization

fiber

Horizontal polarization
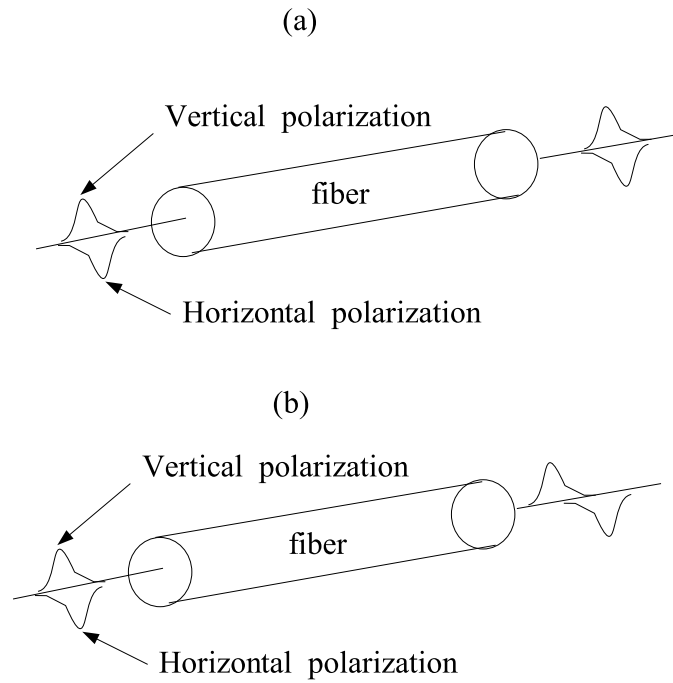
Figure 1.2: Single-mode fiber. (a) Ideal fiber: the light travelling along two polarization axes move at the same speed; (b) Real fiber: the light travelling along one polarization axis moves slower or faster than the light polarized along the other axis.

PMD area include PMD measurement, characterization, modelling, emulation, and compensation. This thesis addresses PMD modelling and PMD compensation.

1.2 Contributions of this Thesis

Again, the broad objectives of this thesis are to understand time-varying dispersive communication channels, and to develop algorithms and heuristics that enable high data rate multimedia transmissions over these channels. The main contributions made in this thesis are:

1. A novel model that maps a dispersive fiber optic channel into a one-input two-output system. This new description not only conveys an alternative view of the PMD effects on transmitted signals, but also allows traditional training and equalization techniques to be applied in PMD compensation.

2. An original approach that enables a training-based low-complexity compensation of the first-order polarization mode dispersion.

3. A fast algorithm that reduces the peak-to-average power ratio of OFDM signals with low overhead.

4. An extensive comparison of frequency offset tracking algorithms for OFDM systems.

5. Closed-form expressions of the optimal training length as a function of packet length and signal-to-noise ratio. The results are valid for OFDM-based anytime anywhere wireless mobile communication systems, and lead to low-cost adaptive training length control for achieving a maximum system throughput at medium and high SNR.

1.3 Organization of this Thesis

The remainder of this thesis is organized as follows.

Chapter 2 reports a new model for fiber optic channels subject to polarization mode dispersion. Section 2.2 gives a brief introduction to the PMD phenomenon and reviews two traditionally used mathematical descriptions of PMD. Section 2.3 derives the proposed 2-dimensional PMD channel response. Section 2.4 demonstrates the PMD channel response for a simulated fiber. Section 2.5 further shows how to find the corresponding PMD channel response from a given PMD vector.

Chapter 3 proposes a new algorithm that compensates the first-order PMD at very low cost. Section 3.2 revisits the first-order PMD. Section 3.3 gives a brief description of the existing continuously tunable first-order PMD compensator (FOPMDC). Sections 3.4 introduces the new discretely tunable FOPMDC. Finally, Section 3.5 discusses simulation results to show the utility of the new scheme.

Chapter 4 introduces a novel orthogonal projection-based partial transmit sequence (OPPTS) method for peak-to-average power ratio reduction in OFDM systems. Section 4.2 briefs the OFDM modulation and the peak-to-average power ratio properties of OFDM signals. Section 4.3 revisits the existing partial transmit sequence (PTS) scheme. Section 4.4 presents a geometrical interpretation to combining in any PTS approach and proposes the new scheme. The computational complexity as well as performance of the proposed method are evaluated and compared with other methods in Section 4.5.

Chapter 5 compares frequency offset tracking algorithms for an OFDM-based wireless mobile system. Section 5.2 presents the system model. Section 5.3 revisits the principles of the pilot tone-aided (PTA) method and the cyclic prefix-based (CPB) approach. Two modifications that were found necessary are proposed for the algorithms. Section 5.4 evaluates and compares PTA and CPB schemes in simulation.

Chapter 6 investigates the optimal training length for OFDM systems under varying channel conditions. Section 6.2 describes the system model used in the chapter. Section 6.3 analyzes and quantifies the impact of the training length on the system throughput. Section 6.4 derives closed-form expressions of the optimal training length at medium and high SNR, and verifies the results in simulation. Section 6.5 gives concluding remarks.

Chapter 7 concludes this thesis, summarizing its findings and suggesting possible topics for future research.

CHAPTER 2

Channel Representation of Single-Mode Fibers with Polarization-Mode Dispersion

2.1 Introduction

As the speeds of optical communication systems grow higher than 10 Gbit/s, polarization mode dispersion (PMD) in single-mode fibers becomes a dominant limiting factor to system performance [2]-[8]. Polarization mode dispersion is caused by asymmetry in the fiber core and cladding. Light propagation in single-mode fibers is governed by two orthogonally polarized modes. In the case of imperfect fibers, the two modes are no longer degenerate, resulting in pulse broadening and system penalties. The PMD's statistical nature makes it difficult to compensate.

To overcome the PMD-induced impairments in future high-speed optical networks, various strategies have been under active investigation [9]-[13]. In principle these methods can be divided into two classes. One class emulates the characteristics of complementary fiber PMD, using a series of birefringent fibers connected by adjustable polarization controllers. The other is built on the classic inter-symbol interference (ISI) cancellation technique where linear equalizers are employed. To apply methods of the first type, it is essential to know the statistical characteristics of PMD parameters, including the principal states of polarization (PSP) and the differential group delay (DGD) [7, 14]. The second

approach demands knowledge of PMD channel response for determining filter length, filter tap spacing, and filter tap weight ranges. PMD channel response, however, has not been characterized.

In this chapter, we define an equivalent baseband single-input two-output representation for a single-mode fiber with PMD. This new description conveys an alternative view of the PMD effects on transmitted signals, and provides explicit information for the design of linear equalizers, both for initialization and channel estimation-based adaptation. We begin with a brief introduction in Section 2.2 to two widely adopted mathematical representations of PMD. Section 2.3 derives the proposed 2-dimensional PMD channel response. Section 2.4 demonstrates the PMD channel response for a simulated fiber. In Section 2.5, we further show how to find the corresponding PMD channel response given a polarization dispersion vector. The operation is desirable for the theoretical analysis and simulation study of slowly changing PMD. Other impairments such as polarization-dependent loss (PDL), polarization-dependent gain (PDG), fiber nonlinearities, and chromatic dispersion are not considered here.

2.2 Traditional Mathematical Descriptions of PMD

There are two popularly used mathematical descriptions for the PMD phenomenon. One is the Jones matrix which indicates that the equivalent baseband transmission properties of any linear birefringent fiber can be represented by a 2×2 frequency-dependent complex transformation matrix of the following form [5]:

$$T(\omega) = e^{\alpha(\omega)}U(\omega) = e^{\alpha(\omega)} \begin{bmatrix} u_1(\omega) & u_2(\omega) \\ -u_2^*(\omega) & u_1^*(\omega) \end{bmatrix}, \qquad (2.1)$$

where ω represents the angular frequency deviation from the carrier ω_0, and the superior $*$ indicates transposition and conjugation. $\alpha(\omega), u_1(\omega)$ and $u_2(\omega)$ are complex numbers. Note that $\alpha(\omega)$, which is independent of the state of polarization (SOP), does not contribute to the PMD effects. $u_1(\omega)$ and $u_2(\omega)$ satisfy the relation

$$|u_1|^2 + |u_2|^2 = 1. \tag{2.2}$$

To simulate $U(\omega)$, the fiber is commonly modelled as a concatenation of M polarization-maintaining fibers with varying group delays and orientations of the principal axes [15, 16]. Generally M larger than 100 is required to get realistic PMD statistics. Mathematically $U(\omega)$ is given by

$$U(\omega) = \prod_{i=1}^{M} P_i(\omega) \cdot D_i, \tag{2.3}$$

with

$$P_i(\omega) = \begin{pmatrix} e^{j\frac{\Delta\tau_i}{2}\omega} & 0 \\ 0 & e^{-j\frac{\Delta\tau_i}{2}\omega} \end{pmatrix},$$

and

$$D_i = \begin{pmatrix} \cos(\theta_i)e^{j\phi_i/2} & \sin(\theta_i)e^{j\phi_i/2} \\ -\sin(\theta_i)e^{-j\phi_i/2} & \cos(\theta_i)e^{-j\phi_i/2} \end{pmatrix}.$$

Here $\Delta\tau_i$ represents the group delay induced by the ith section, and is generated following a uniform distribution in this chapter. D_i gives a frequency-independent coordinate transformation of the principal axes. θ_i and ϕ_i respectively denote the random polarization and phase angle, and are randomly generated following a uniform distribution with $\theta_i \in [0; 2\pi)$ and $\phi_i \in [-\pi/2; \pi/2]$.

The other PMD representation is called the principal states model, developed by Poole and Wager [5]. It states that for every frequency component of a fiber, there are two special polarization states, called the principle states of polarization (PSPs). And for each pairs of PSPs at the fiber input, there is a corresponding

11
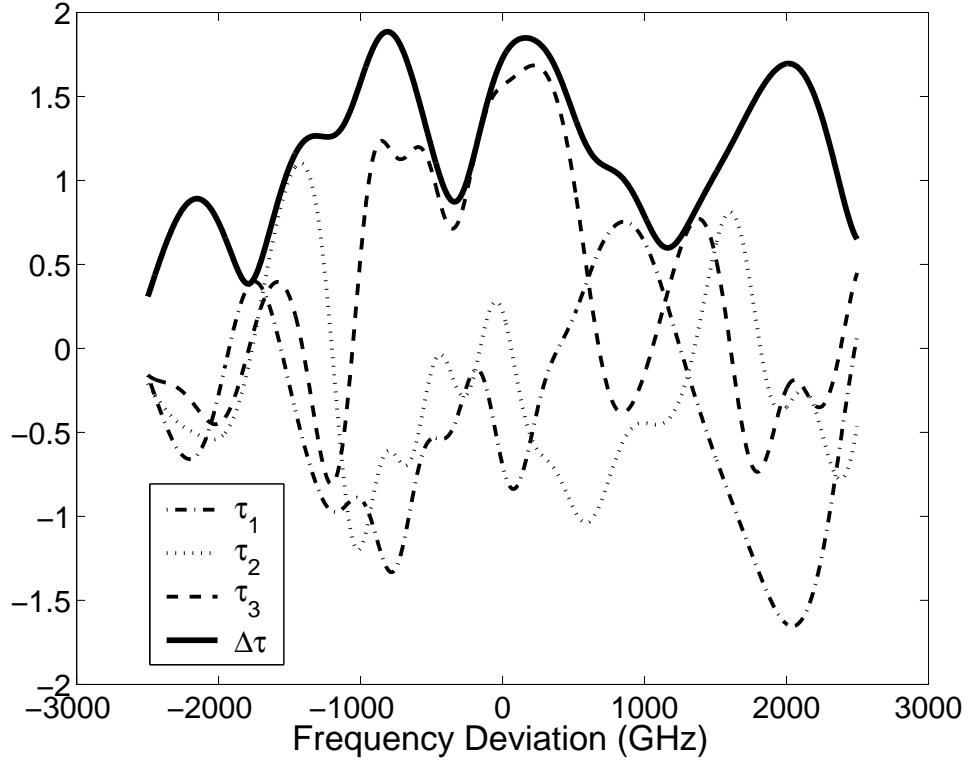
Figure 2.1: Simulated DGD and PMD vector components as a function of frequency deviation from the optical carrier. The unit of DGD is picosecond.

pair of PSPs at the fiber output. The input and output PSPs are related by the fiber's transmission matrix. Using the principal states model, PMD can be described more concisely by the PMD vector:

$$\vec{\tau}(\omega) \equiv \Delta\tau(\omega) \cdot \hat{p}(\omega). \tag{2.4}$$

Here the magnitude $\Delta\tau$ indicates the differential group delay (DGD), and the direction $\hat{p}$, a Stokes vector, represents the slow output PSP. Given $U(\omega)$, $\vec{\tau}(\omega)$ can be easily derived [4]. Fig. 2.1 shows an example of the PMD vector as a function of frequency deviation from the optical carrier.

We emphasize that DGD and PSP's are functions of ω, though in the literature

12

their meaning is often limited to the first-order PMD, i.e., DGD and PSP's at ω_0. To facilitate our analysis, we label the Jones vectors representing the fast and the slow output PSP's at ω_0 as $\vec{e}_O^f$ and $\vec{e}_O^s$, respectively. They correspond to the eigenstates of the matrix $U_\omega U^{-1}$ evaluated at ω_0 [5]. The subscript ω indicates differentiation over ω. The superior -1 represents inversion. Likewise, denote the Jones vectors representing the pair of input PSP's at ω_0 as $\vec{e}_I^f$ and $\vec{e}_I^s$, each of which is simply $U^{-1}(\omega_0)$ times the corresponding output PSP. The difference between the imaginary parts of the two eigenvalues of $U_\omega U^{-1}$ at ω_0 gives $\Delta\tau(\omega_0)$. The first-order PMD vector is then

$$\vec{\tau}(\omega_0) \equiv \Delta\tau(\omega_0) \cdot \hat{p}(\omega_0), \tag{2.5}$$

where $\hat{p}(\omega_0)$ is the counterpart of $\vec{e}_O^s$ in Stokes space.

2.3 One-Input Two-Output Representation of Single-Mode Fibers with PMD

In principle, linear equalization for mitigating PMD can be deployed in either the electrical domain, as shown in Fig. 2.2, or the optical domain, as shown in Fig. 2.3. Since electronic equalizers in direct detection systems are subject to the loss of the phase information [17], various optical equalizers have been proposed. [20] discussed a novel optical lattice filter approach aiming at all-order PMD compensation, based on the analysis of the polarization trajectories on the Poincaré Sphere. The dynamic control of filter parameters, however, demands a careful and sophisticated design. [21] presented a simulation-based study of an adaptive optical equalizer for combating PMD, chromatic dispersion, and self-phase modulation. Using the eye-opening penalty as the performance criterion and employing a nonlinear optimization method, the paper shows that significant
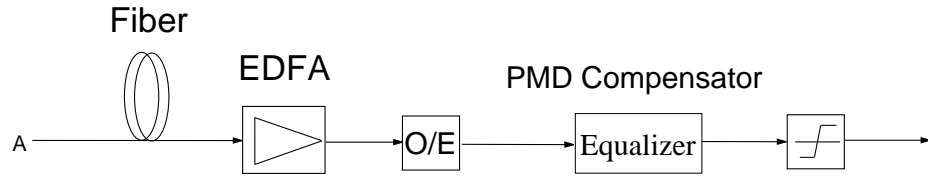
Figure 2.2: Fiber optical transmission system with an electronic PMD compensator.
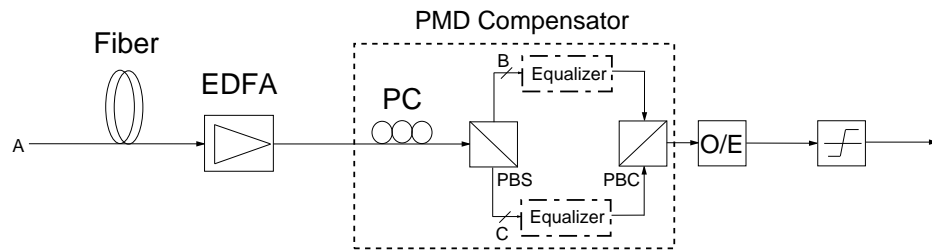
Figure 2.3: Fiber optical transmission system with a 2-path optical PMD compensator.

performance improvement can be achieved with the proposed equalizer. The paper also pointed out the importance of optimizing the filter order and the filter tap spacing, but did not provide a general guidance for doing so.

In this chapter, we develop a one-input two-output channel representation for a single-mode fiber with PMD in the context of an optical PMD compensator. The derived channel response can provide direct information for determining the optical equalizer length, the tap spacing and the tap weight ranges. It is also useful for the design of electronic equalizers.

As shown in Fig. 2.3, the modulated optical signal is transmitted through one or more fiber spans with erbium-doped fiber optical amplifiers (EDFA), and

14

finally goes through the PMD compensator, before being detected. The PMD compensator is formed by a two-path optical line with one linear equalizer on each path, a polarization beam splitter (PBS) at input, a polarization beam combiner (PBC) at output, and a polarization controller (PC) before the PBS. The PC rotates the time-varying output PSP's, $\vec{e}_O^f$ and $\vec{e}_O^s$, of the fiber at ω_0 into the fixed principal axes of the compensator. The PBS separates the output pulse from the PC into two orthogonally polarized components, which are then reshaped by the equalizers before being recombined.

Clearly the design of the equalizers requires knowledge of both paths in Fig. 2.3, one from A to B, and the other from A to C. Denote the transfer function from A to B as $C^f(\omega)$, and that from A to C as $C^s(\omega)$. An equivalent baseband one-input two-output PMD channel can be then defined with its 2-dimensional frequency response as

$$C(\omega) = \left[\begin{array}{c} C^f(\omega) \\ C^s(\omega) \end{array} \right]. \tag{2.6}$$

To derive $C(\omega)$ from $U(\omega)$, the input and output optical fields of the fiber need to be specified first. Since any optical pulse in a single-mode fiber can be expressed as the vector sum of a pair of orthogonal states of polarization, a well-polarized input field may be then described in terms of the input PSP's at ω_0 by

$$\vec{E}_I(\omega) = (1 - r)\vec{e}_I^f + r\vec{e}_I^s, \tag{2.7}$$

where $r \in [0, 1]$ specifies the relative power along $\vec{e}_I^s$. It can be seen that the defined input field is independent of ω. In other words, all frequency components in an input signal will have the same power-splitting ratio r.

Assume the fiber loss is polarization-independent and the chromatic dispersion

15

is completely compensated. The optical pulse at the output of the fiber is related to $U(\omega)$ by

$$\vec{E}_O(\omega) = a(\omega)e^{\psi(\omega)}U(\omega)\vec{E}_I(\omega),$$

where $a(\omega)e^{\psi(\omega)}$ is the frequency domain representation of the input signal. Setting $a(\omega)e^{\psi(\omega)}$ to 1, which is equivalent to transmitting a single short pulse, we obtain

$$\vec{E}_O(\omega) = U(\omega)\vec{E}_I(\omega). \tag{2.8}$$

$\vec{E}_O(\omega)$ conveys complete information about the PMD channel. Similarly to $\vec{E}_I(\omega)$, $\vec{E}_O(\omega)$ can be expressed as a vector sum of $\vec{e}_O^f$ and $\vec{e}_O^s$, that is

$$\vec{E}_O(\omega) = \hat{C}^f(\omega)\vec{e}_O^f + \hat{C}^s(\omega)\vec{e}_O^s. \tag{2.9}$$

Here $\hat{C}^f(\omega)$ indicates the component along $\vec{e}_O^f$, and $\hat{C}^s(\omega)$ indicates the component along $\vec{e}_O^s$. The frequency-dependency of $\hat{C}^f(\omega)$ and $\hat{C}^s(\omega)$ implies the existence of high-order PMD. We shall argue that $\hat{C}^f(\omega)$ and $\hat{C}^s(\omega)$ are identical to $C^f(\omega)$ and $C^s(\omega)$, respectively.

It can be seen from Equations (2.8) and (2.9), that $\hat{C}^f(\omega)$ and $\hat{C}^s(\omega)$ are actually the projection of $\vec{E}_O(\omega)$ onto $\vec{e}_O^f$ and $\vec{e}_O^s$ respectively. Note that $C^f(\omega)$ and $C^s(\omega)$ are defined as the components along the fixed axes of the compensator, and a polarization controller has been employed to rotate $\vec{e}_O^f$ and $\vec{e}_O^s$ into the fixed ones. Therefore $\hat{C}^f(\omega)$ and $\hat{C}^s(\omega)$ are respectively identical to $C^f(\omega)$ and $C^s(\omega)$, and can be calculated through the following projection operations,

$$C^f(\omega) = \frac{\vec{e}_O^{f*}\vec{E}_O(\omega)}{\vec{e}_O^{f*}\vec{e}_O^f}, C^s(\omega) = \frac{\vec{e}_O^{s*}\vec{E}_O(\omega)}{\vec{e}_O^{s*}\vec{e}_O^s}. \tag{2.10}$$

Clearly $C(\omega)$ is a function of r.

2.4 Numerical Example

In this section, we generate a virtual fiber with the multi-section model detailed in Section II, and then numerically demonstrate its equivalent baseband 1-input 2-output channel representation. The light launch condition is set to $r = 0.5$, in other words, the signal power is equally distributed over the two input principal axes.

Given a randomly generated set $\{\Delta\tau_i, \theta_i, \phi_i, 1 \leq i \leq M\}$, the fiber transformation matrix $U(\omega)$ as well as the input and output PSP's at ω_0 can be derived. $\vec{E}_O(\omega)$ and $C(\omega)$ may be calculated by using Equations (2.8) and (2.10), respectively.

The resulting $C^f(\omega)$ and $C^s(\omega)$ is shown in Fig. 2.4. It can be seen that around the optical carrier frequency (0 on the normalized axis), the magnitude responses of both components are $\sqrt{2}/2$, or equivalently 0.5 in optical power. This launch-condition-determined power distribution at ω_0 coincides with the general understanding that a narrowband signal suffers only the first-order PMD effect. Apart from the carrier frequency, however, severe frequency-dependent power coupling between the two polarization axes is observed. The random power-wandering is due to higher-order PMD.

The time-varying property of the fiber PMD is simulated by employing different sets of $\{\Delta\tau_i, \theta_i, \phi_i, 1 \leq i \leq M\}$ over time. In our simulation, 1000 uncorrelated sets are used. The resulting fiber DGD at ω_0 has a mean of 57 ps and a dynamic range from 10 ps to 117 ps over time. At each static moment, two 6-tap half-bit-period-spaced finite impulse response (FIR) filters, $c^f(n)$ and $c^s(n)$, are designed to approximate the known frequency response, $C^f(\omega)$ and $C^s(\omega)$. The filter structure is shown in Fig. 2.5. The filter order and the tap spacing are
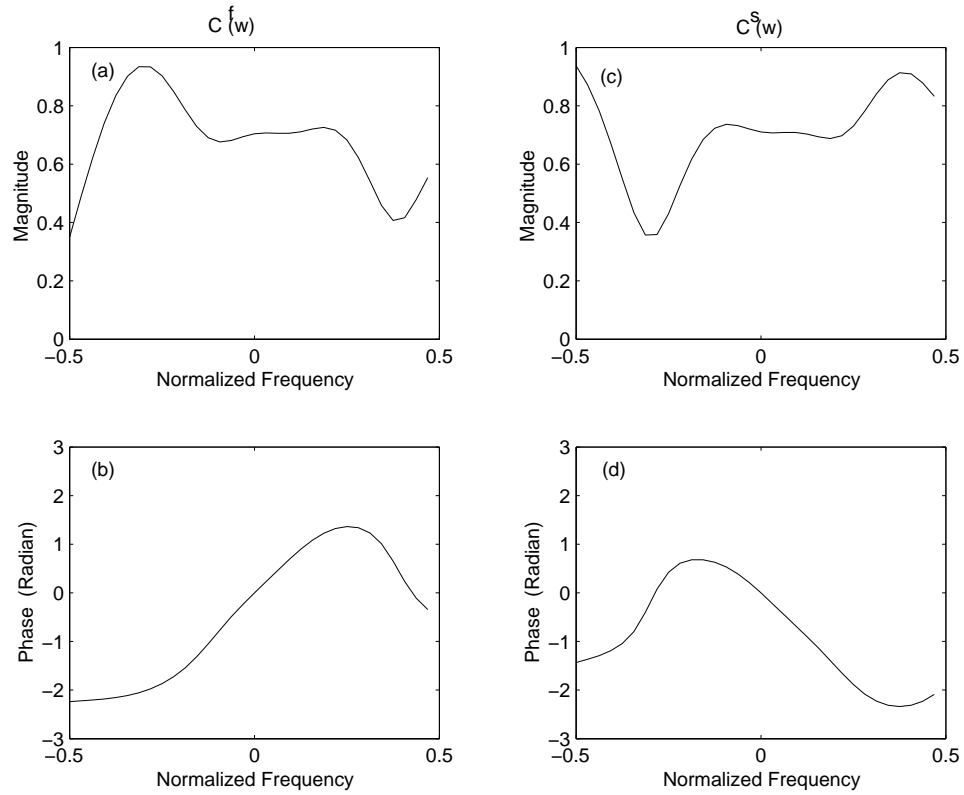
Figure 2.4: Frequency response of a static PMD channel. (a): Magnitude response of $C^f(\omega)$; (b): Phase response of $C^f(\omega)$; (c) Magnitude response of $C^s(\omega)$; (d) Phase response of $C^s(\omega)$.
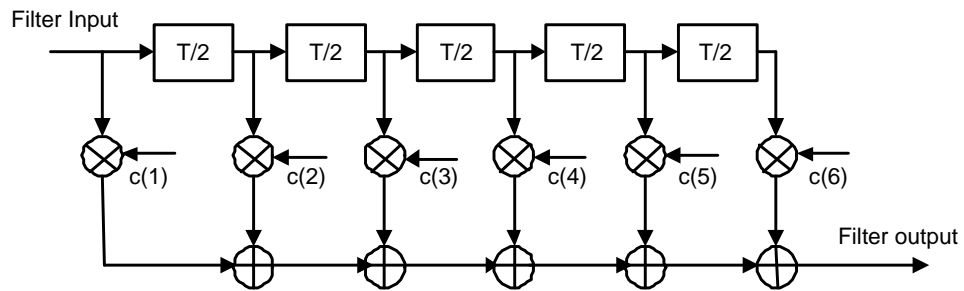
Figure 2.5: Structure of a finite impulse response filter.

jointly determined to have the minimum number of taps while maintaining the approximation error within the acceptable range. The tap weights are then obtained by applying the equal-ripple design. The dynamics of a time-varying PMD channel can be then visualized by showing how each of the filter taps changes over time. Since $\Delta\tau(\omega_0)$ is generally considered as an important parameter for describing the PMD effects, we are particularly interested in how the taps vary with it.

The scatter plots of the coefficients of $c^s(n)$ versus $\Delta\tau(\omega_0)$ are presented, with their real part in Fig. 2.6 and their imaginary part in Fig. 2.7. It can be seen that over the dynamic range of $\Delta\tau(\omega_0)$, both the real and the imaginary parts of Tap 1 and Tap 6 are relatively small. This indicates that a length of 4 is actually sufficient for filters used to represent the simulated PMD channel. This observation gives useful information for determining the length of the equalizers, which is usually required to be longer than that of the channel. Also in Fig. 2.6, each of Taps 3, 4 and 5 has a $\Delta\tau(\omega_0)$-related pattern. Explicitly, Tap 4 is always positive and determines the equalizer-induced delay. And as $\Delta\tau(\omega_0)$ goes up, Tap 3 decreases and Tap 5 increases to generate additional pulse delay. Conversely as $\Delta\tau(\omega_0)$ gets smaller, Tap 3 increases and Tap 5 decreases to reduce the delay introduced by Tap 4. In Fig. 2.7, however, no $\Delta\tau(\omega_0)$-related pattern is observed, the imaginary part of each tap of $c^s(n)$ is randomly distributed in a symmetric region around zero.

Similar observations can be obtained from illustrating $c^f(n)$. The main difference is that Tap 3, rather than Tap 4 of the real part of $c^f(n)$, dominates the equalizer-induced delay. The reason is that the pulse along the fast principal axis is subject to a negative time shift, by the definition of $U(\omega)$. Therefore as $\Delta\tau(\omega_0)$ get larger, Tap 2 increases and Tap 4 decreases to result in more pulse leading.

Now assume the receiver noise has a Gaussian distribution. We design two minimum-mean-squared-error linear equalizers, $w^f(n)$ and $w^s(n)$, to remove the PMD-induced inter-symbol interference. As the effective length of the simulated PMD channel is only 4, the same filter structure in Fig. 2.5 is adopted for equalizers in our simulation study. For each snapshot of the PMD channel, the equalizer coefficients are first designed to approximate the inverse PMD channel and then adjusted to minimize the average difference between the transmitted signal and the received signal. Primary simulation results show that with the optimally designed linear equalizers, the PMD compensator outperforms an ideal first-order PMD compensator by 1.5 dB in the average eye-opening penalty. The scatter plots of the coefficients of $w^s(n)$ are shown in Fig. 2.8 (real part) and Fig. 2.9 (imaginary part). Again, a $\Delta\tau(\omega_0)$-related pattern is observed in Fig. 2.8, meanwhile, in Fig. 2.9 each tap simply scatters over a certain range around zero.

2.5   PMD Inversion: From PMD Vector to Jones Matrix

To perform theoretical analysis and a simulation study of slowly changing PMD, it is desirable to visualize the PMD channel response corresponding to a given polarization dispersion vector. A direct transformation from a dispersion vector to the corresponding PMD channel response is very difficult. Considering the lower-order PMD only, however, a work-around can be found. Fig. 2.10 shows three different representations of PMD, that is, the fiber transformation matrix $U(\omega)$, the polarization dispersion vector $\vec{\tau}(\omega)$, and the 2-dimensional channel $C(\omega)$. Conversions I and II have been discussed in Sections 2.3 and 2.4 respectively. To alternatively achieve Conversion III, we propose to find the fiber transformation matrix from a dispersion vector first, then derive the corresponding PMD channel response by applying Conversion II. Since the lower-order PMD usually
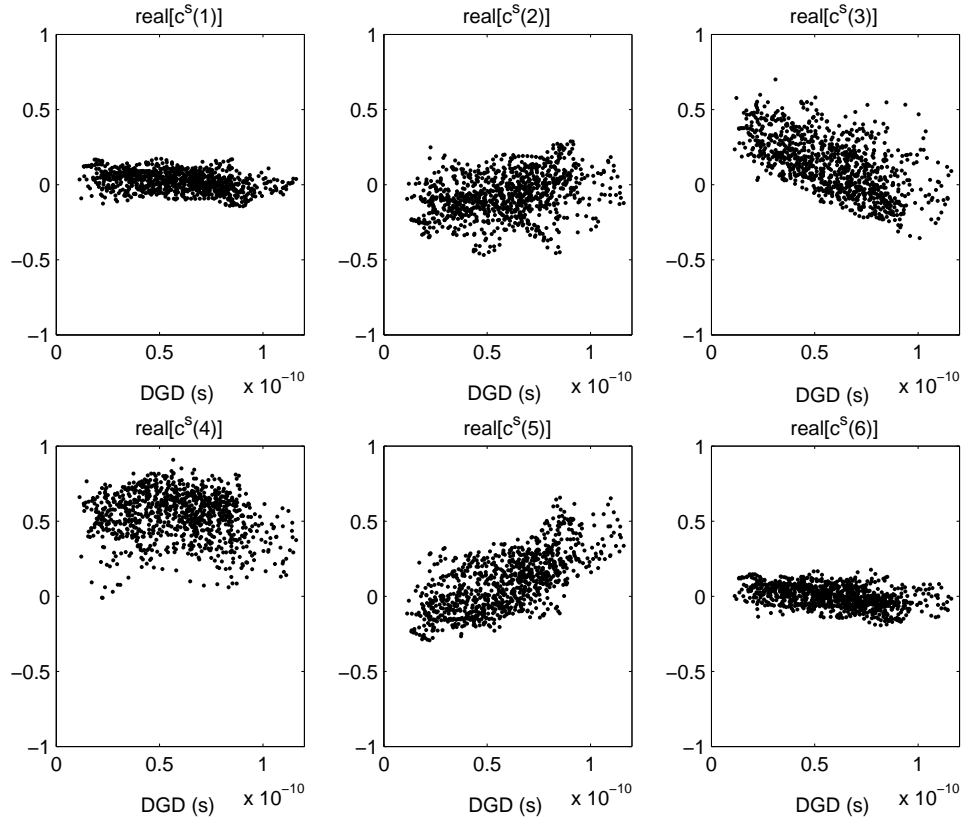
Figure 2.6: Scatter plot of the real part of $c^s(n)$ versus $\Delta\tau(\omega_0)$.
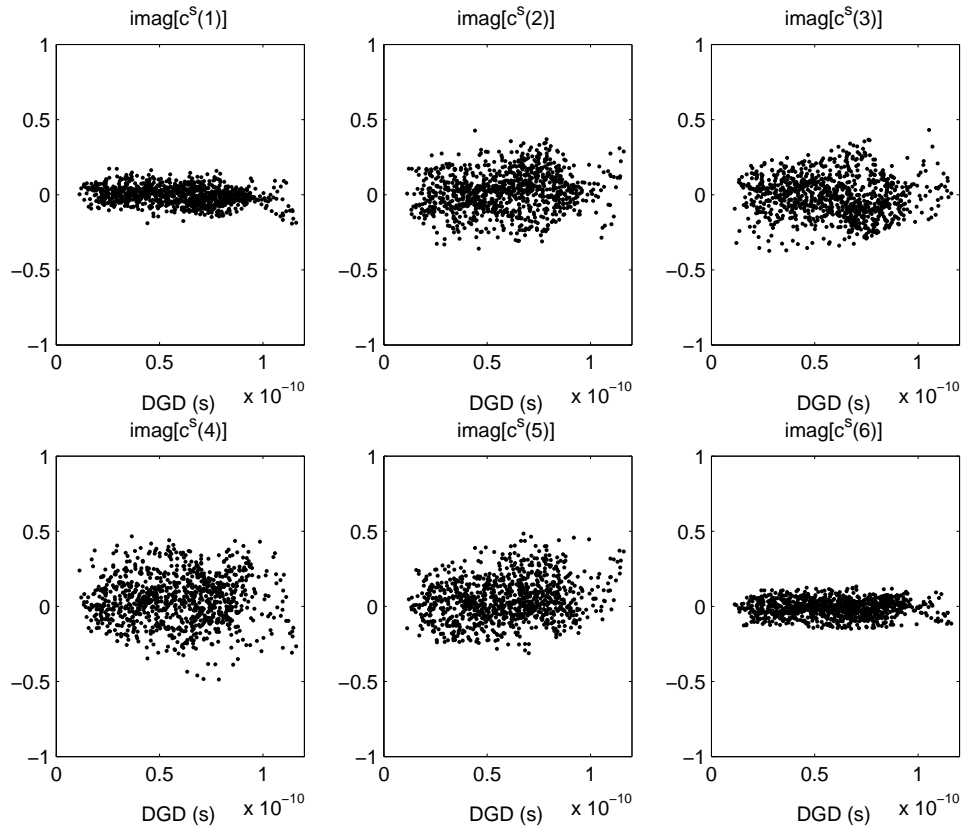
Figure 2.7: Scatter plot of the imaginary part of $c^s(n)$ versus $\Delta\tau(\omega_0)$.
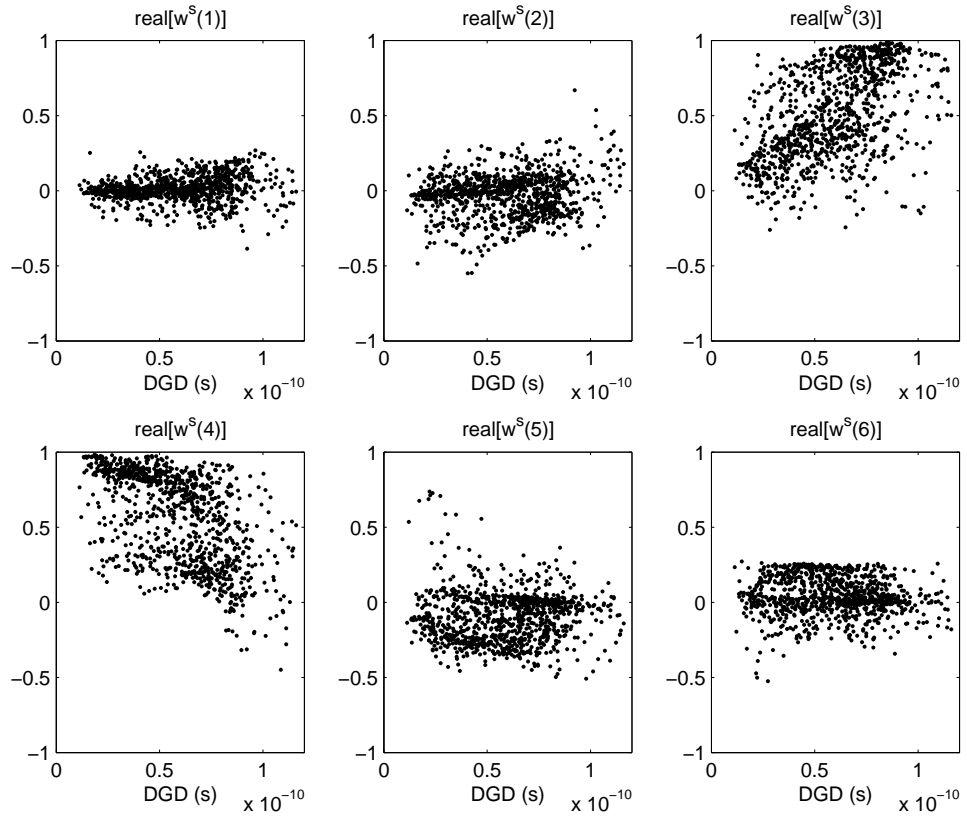
Figure 2.8: Scatter plot of the real part of $w^s(n)$ versus $\Delta\tau(\omega_0)$.
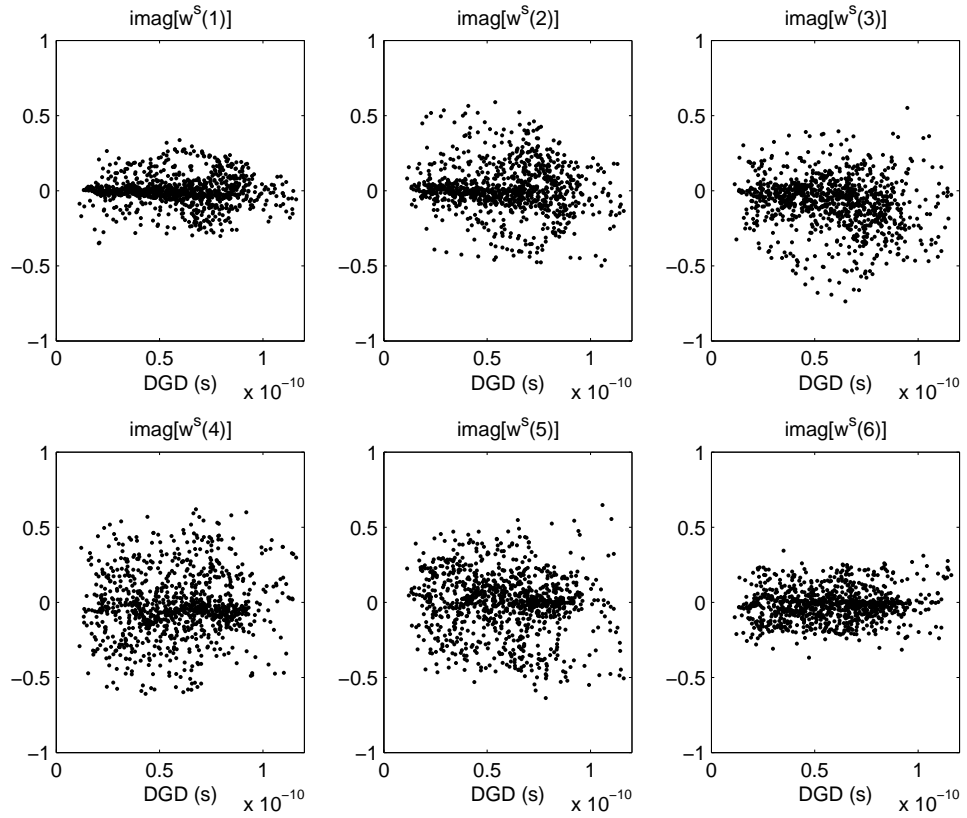
Figure 2.9: Scatter plot of the imaginary part of $w^s(n)$ versus $\Delta\tau(\omega_0)$.
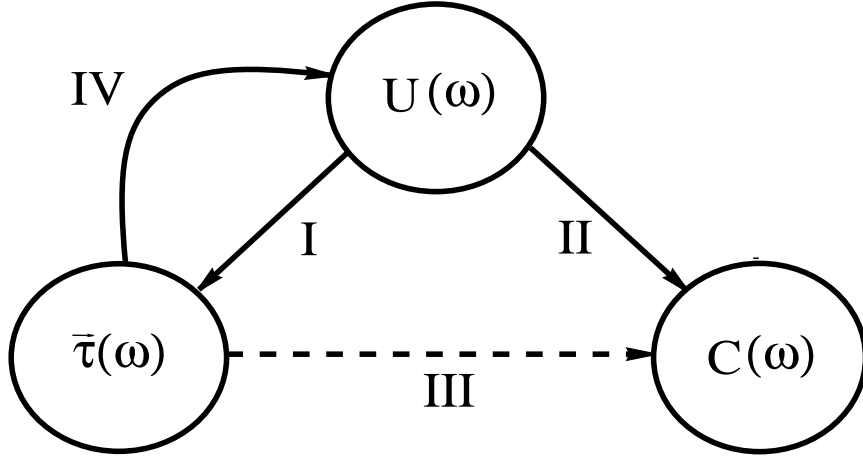
Figure 2.10: Different representations of PMD

dominates the PMD-induced distortion, this approximation is meaningful.

In order to find $U(\omega)$ from $\vec{\tau}(\omega)$, first apply a similarity transformation to $U_\omega U^{-1}$, i.e.,

$$U_\omega U^{-1}(\omega) = R(\omega) \begin{pmatrix} \frac{1}{2}j\Delta\tau(\omega) & 0 \\ 0 & -\frac{1}{2}j\Delta\tau(\omega) \end{pmatrix} R^{-1}(\omega), \qquad (2.11)$$

where $R(\omega)$ denotes a 2×2 special unitary matrix rotating the coordinate axes in the vector space of polarization states to the principal axes of the fiber at frequency ω. Applying Taylor's expansion to $R(\omega)$ and $\Delta\tau(\omega)$ up to first order, we have

$$R(\omega) = R^0 + R^0_\omega \cdot \omega, \qquad (2.12)$$

and

$$\Delta\tau(\omega) = \Delta\tau^0 + \Delta\tau^0_\omega \cdot \omega. \qquad (2.13)$$

Here $\Delta\tau^0$ denotes the DGD, $\Delta\tau^0_\omega$ represents the rate of the change in DGD, R^0 relates to the principal axes, and R^0_ω relates to the rate of the change in the prin-

cipal axes, all evaluated at ω_0. Given R^0, $\Delta\tau^0$, $\Delta\tau_\omega^0$ and R_ω^0, the transformation matrix $U(\omega)$ can be then solved by integrating $U_\omega U^{-1}$ over ω.

As follows the $U(\omega)$ is derived for different scenarios. For simplicity, hereafter we assume that $R^0 = I_{2\times 2}$, which can be achieved by carefully choosing the coordinate axes so that it superimposes on the output principal axes of the fiber. We may also assume $U(\omega_0) = I_{2\times 2}$, which means that a common rotation on all frequency components is ignored in evaluating the PMD effects. Therefore the input PSP's are mathematically the same as the output PSP's at ω_0, and both can be written as the pair of $\begin{pmatrix} 1 \\ 0 \end{pmatrix}$ and $\begin{pmatrix} 0 \\ 1 \end{pmatrix}$. Note that the above two assumptions facilitate the derivation but do not hide any PMD effects. Explicitly write $U(\omega)$ as

$$U(\omega) = \begin{pmatrix} u_1(\omega) & u_2(\omega) \\ -u_2^*(\omega) & u_1^*(\omega) \end{pmatrix}. \tag{2.14}$$

The off-diagonal terms in $U(\omega)$ now represent power coupling between the two principal axes.

Case 1: $\Delta\tau_\omega^0 = 0$ and $R_\omega^0 = O$ (O is an all-zeros matrix) give

$$U_\omega U^{-1}(\omega) = \begin{pmatrix} \frac{1}{2}j\Delta\tau^0 & 0 \\ 0 & -\frac{1}{2}j\Delta\tau^0 \end{pmatrix}. \tag{2.15}$$

Integrating both sides of Equation (2.15) over ω, we have

$$U(\omega) = \begin{pmatrix} e^{\frac{1}{2}j\Delta\tau^0 \cdot \omega} & 0 \\ 0 & e^{-\frac{1}{2}j\Delta\tau^0 \cdot \omega} \end{pmatrix}. \tag{2.16}$$

Obviously there is no power coupling between the slow and the fast principal axes, which indicates the first-order PMD effect.

Case 2: $\Delta\tau_\omega^0 \neq 0$ and $R_\omega^0 = O$. From

$$U_\omega U^{-1}(\omega) = \begin{pmatrix} \frac{1}{2}j\Delta\tau(\omega) & 0 \\ 0 & -\frac{1}{2}j\Delta\tau(\omega) \end{pmatrix},$$ (2.17)

we find that

$$U(\omega) = \begin{pmatrix} u_1(\omega) & 0 \\ 0 & u_1^*(\omega) \end{pmatrix},$$ (2.18)

with $u_1(\omega) = e^{\frac{1}{2}j\left(\Delta\tau^0\cdot\omega + \frac{1}{2}\Delta\tau_\omega^0\cdot\omega^2\right)}$. Again, there is no coupling between the slow and the fast principal axes. However, the phase in this case is no longer a linear but a quadratic function of ω, which corresponds to the so-called polarization-dependent chromatic dispersion effect, part of the second-order PMD impact.

Case 3: $\Delta\tau_\omega^0 = 0$ and $R_\omega^0 \neq O$. To clarify this case, we rewrite the term R_ω^0 as

$$R_\omega^0 = -\frac{1}{2}j\sum_{i=1}^{3} a_i\sigma_i.$$ (2.19)

where σ_1, σ_2, and σ_3 are 2×2 Pauli spin matrices defined as

$$\sigma_1 = \begin{pmatrix} 1 & 0 \\ 0 & -1 \end{pmatrix}, \sigma_2 = \begin{pmatrix} 0 & 1 \\ 1 & 0 \end{pmatrix}, \sigma_3 = \begin{pmatrix} 0 & -j \\ j & 0 \end{pmatrix}.$$

$a_i, i = 1, 2, 3$, describe the rate of the change in PSP at ω_0. Plugging the expression (2.19) into Equation (2.11) and noticing that $[I + R_\omega^0 \cdot \omega]^{-1}$ is equivalent to $I - R_\omega^0 \cdot \omega$ up to linear order, we arrive at the expression

$$U_\omega U^{-1}(\omega) = \frac{1}{2}j\Delta\tau^0\sigma_1 + \frac{1}{2}j\Delta\tau^0(a_3\sigma_2 - a_2\sigma_3)\cdot\omega,$$ (2.20)

or equivalently

$$\ln U(\omega) = \frac{1}{2}j\Delta\tau^0\omega\left[\sigma_1 + \frac{1}{2}a_3\sigma_2\cdot\omega - \frac{1}{2}a_2\sigma_3\cdot\omega\right].$$ (2.21)

By defining

$$\hat{r} \equiv \begin{pmatrix} r_1 \\ r_2 \\ r_3 \end{pmatrix} = \frac{1}{A} \begin{pmatrix} -1 \\ -\frac{1}{2}a_3\cdot\omega \\ \frac{1}{2}a_2\cdot\omega \end{pmatrix},$$

and

$$\phi = \Delta\tau^0 \omega \cdot A,$$

with

$$A = \sqrt{1 + \frac{1}{4}a_3^2 \cdot \omega^2 + \frac{1}{4}a_2^2 \cdot \omega^2},$$

we have

$$\ln U(\omega) = -\frac{1}{2}j\phi\hat{r} \cdot \vec{\sigma}. \tag{2.22}$$

Here $\hat{r}$ is a 3-dimensional unit Stokes vector representing the rotation axis of $U(\omega)$, ϕ is the rotation angle around $\hat{r}$, and $\hat{r} \cdot \vec{\sigma} = r_1\sigma_1 + r_2\sigma_2 + r_3\sigma_3$. Using the exponential formula for a general Pauli Spin matrix [4], we arrive at $U(\omega)$ from Equation (2.22) as follows

$$\begin{pmatrix} \cos(\phi/2) - jr_1\sin(\phi/2) & j(r_2 + jr_3)\sin(\phi/2) \\ j(r_2 - jr_3)\sin(\phi/2) & \cos(\phi/2) + jr_1\sin(\phi/2) \end{pmatrix}. \tag{2.23}$$

Clearly coupling exists between the slow and the fast axes, which explains the system impact of another part of the second-order PMD, depolarization.

Case 4: $\Delta\tau_\omega^0 \neq 0$ and $R_\omega^0 \neq O$, which together represent a more realistic situation, give

$$U_\omega U^{-1}(\omega) = \frac{1}{2}j\Delta\tau^0\sigma_1 + \frac{1}{2}j\Delta\tau_\omega^0 \cdot \omega \cdot \sigma_1 \tag{2.24}$$

$$+\frac{1}{2}j\Delta\tau^0(a_3\sigma_2 - a_2\sigma_3) \cdot \omega,$$

we then arrive at

$$\ln U(\omega) = \frac{1}{4}j\Delta\tau_\omega^0 \cdot \omega^2 \cdot \sigma_1 \tag{2.25}$$

$$+\frac{1}{2}j\Delta\tau^0 \cdot \omega \cdot \left(\sigma_1 + \frac{\omega}{2}a_3\sigma_2 - \frac{\omega}{2}a_2\sigma_3\right).$$

The resulting $U(\omega)$ has the same form as (2.23) with $\hat{r}$ and ϕ defined as

$$\hat{r} = \frac{1}{B} \begin{pmatrix} -1 - \frac{\Delta\tau_\omega^0}{2\Delta\tau^0} \cdot \omega \\ -\frac{1}{2}a_3 \cdot \omega \\ +\frac{1}{2}a_2 \cdot \omega \end{pmatrix},$$

and

$$\phi = \Delta\tau^0 \cdot \omega \cdot B,$$

where

$$B = \sqrt{\left(1 + \frac{1}{2}\frac{\Delta\tau_\omega^0}{\Delta\tau^0} \cdot \omega\right)^2 + \frac{1}{4}a_3^2 \cdot \omega^2 + \frac{1}{4}a_2^2 \cdot \omega^2}.$$

As stated at the beginning of this section, the corresponding two-dimensional PMD channel response $C(\omega)$ can be therefore found from $U(\omega)$ by using the procedure described in Section 2.3.

2.6 Conclusion

We have derived and numerically demonstrated an equivalent single-input two-output baseband representation for fiber optic channels with PMD. The two-dimensional channel response provides straightforward information to the design of linear equalizers aiming to suppress the PMD effects. A relationship between the polarization dispersion vector and the PMD channel response is also detailed, which may also be used to analyze the system impacts of PMD up to second order. Future work will focus on the equalizer design.

CHAPTER 3

Low-Cost Compensation of First-Order Polarization Mode Dispersion

3.1 Introduction

In order to make high-speed signal transmission feasible in fibers subject to severe PMD effects, various strategies, including optical [9], electronic [12], and opto-electronic signal processing [24] are being considered.

For first-order PMD mitigation, three methods have been discussed in the literature. The first approach, employing an electronic transversal filter, works well in principle but requires tedious multi-parameter optimizations and adaptations [16]. The second strategy, often referred to as the principal state of polarization (PSP) launch [18], suppresses the first-order PMD effects by transmitting signals over only one of the two principal axes of a fiber. This technique is infeasible in long-haul systems owing to the need for a feedback loop from the receiver to the transmitter. The third solution, using a continuously tunable two-path optical delay line, implemented with either free-space optics or nonlinearly-chirped fiber Bragg grating [19], is shown to be very promising. However, the complexity of its control mechanism is rather high.

In this chapter, we propose a low-complexity discretely tunable optical approach, which achieves PMD mitigation as efficiently as does the continuously

tunable counterpart. The rest of this chapter is organized as follows. Section 3.2 revisits the first-order PMD. Section 3.3 gives a brief description of the continuously tunable first-order PMD compensator (FOPMDC). Sections 3.4 introduces the new discretely tunable FOPMDC. Finally, Section 3.5 discusses simulation results to show the utility of the new scheme. Other fiber-related impairments, such as chromatic dispersion, polarization dependent loss, polarization dependent gain and fiber nonlinearities, are not considered in this study.

3.2   Effect of the First-Order PMD

In a single-mode fiber, an arbitrarily polarized optical wave can be represented as a linear superposition of two orthogonal polarization modes. PMD occurs when the transmission speeds of the two modes are distinct due to the loss of circular symmetry in the fiber [2]. PMD is time- and frequency-dependent, and is commonly described by a time-varying three-dimensional dispersion vector, $\vec{\tau}(\omega) = \Delta\tau(\omega) \cdot \hat{p}(\omega)$, where the magnitude $\Delta\tau$ denotes the differential group delay (DGD) between output PSP's, and the unit Stokes vector $\hat{p}$ represents the slow output PSP on the Poincaré sphere. The first-order PMD is defined to be the dispersion vector at the optical carrier frequency ω_0, i.e., $\vec{\tau}(\omega_0) = \Delta\tau(\omega_0) \cdot \hat{p}(\omega_0)$. A higher-order PMD is described by the derivative, $\vec{\tau}_{n\omega}(\omega_0) = \frac{d^n \vec{\tau}(\omega)}{(d\omega)^n}|_{\omega=\omega_0}, n \geq 1$, where the subscript ω indicates differentiation. The bandwidth limitations of higher-order PMD vectors are examined in [23]. They provide important guidance on PMD measurement and PMD compensation in the frequency-domain.

In the time domain, the first-order PMD dispersion effect is manifested by the two components along the two input PSP's being separated in time at the fiber output by the DGD $\Delta\tau(\omega_0)$. Therefore to compensate PMD to the first order, we may simply delay one component with respect to the other by $\Delta\tau(\omega_0)$.

31

However, the detection of $\Delta\tau(\omega_0)$ is not a trivial task.

3.3   The Traditional Continuously Tunable FOPMDC

Fig. 3.1 shows a fiber optic transmission system using a continuously tunable FOPMDC [16]. The modulated optical signal is transmitted through one or more fiber spans with erbium-doped fiber optical amplifiers (EDFA), and finally goes through the PMD compensator, before being detected. The PMD compensator is based on an adjustable two-path optical delay line with a polarization beam splitter (PBS) at input, a polarization beam combiner (PBC) at output, and a polarization controller (PC) before the polarization beam splitter. The polarization controller rotates the time-varying output PSP's of the transmission fiber into the fixed principal axes of the compensator. The PBS separates the output pulse from the PC into two orthogonally polarized components which are then delayed relative to each other by a variable time $\Delta\tau_c$ before they are recombined.
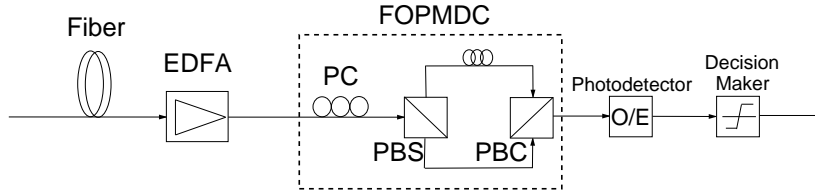
Figure 3.1: Fiber optical transmission system using a continuously tunable FOP-MDC.

To achieve satisfactory first-order PMD compensation, the delay time $\Delta\tau_c$ should be adapted to the time-varying $\Delta\tau(\omega_0)$. Since it is difficult to measure $\Delta\tau(\omega_0)$ directly, the PMD-induced sensitivity is often observed by measuring the power of a few frequency components extracted from the electrical baseband
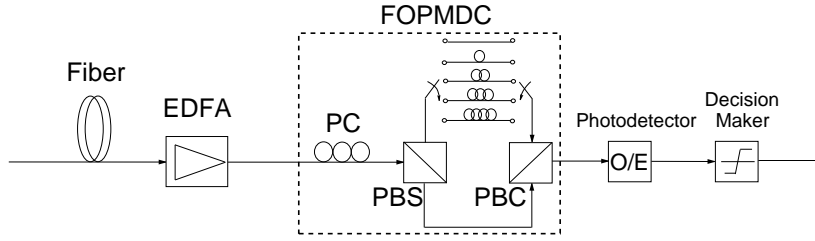
Figure 3.2: Fiber optical transmission system using a discretely tunable FOP-MDC.

signal, using narrow bandpass filters [9]. A linear combination of the filter output signals is then maximized with a gradient-based optimization algorithm so as to minimize the bit error rate (BER).

No doubt both the narrow bandpass filtering and the search for the optimal linear combination raise challenges to the design of such a compensator. Moreover, the gradient-based peak searching may drop into local minima, and therefore minima-escaping tools have to be used, which further complicates the control mechanism.

3.4   The New Discretely Tunable FOMPMDC

To improve over the above scheme, we propose a discretely tunable optical delay line which employs a set of parallel delay paths, each of which generates a fixed delay, as shown in Fig. 3.2. Compared to the continuously adjustable delay line, this discretely tunable alternative has lower hardware complexity and requires a much simpler control mechanism. With the new compensator, the transmission system shall work consecutively in two modes: compensator training, for determining the optical path to use, and data transmission. In the training mode, a

known pseudo-random binary sequence (PRBS) is transmitted. After the polarization controller rotates the fiber output PSP's into the compensator principal axes and the pulse is split into two orthogonal components, the signal along the fast principal axis is fed into the delay paths, one at a time. By combining each delayed signal with the component over the slow principal axis, the path-related eye-opening penalty (EOP) can be then monitored. The optimal delay path is the path generating the minimum penalty. In the transmission mode, the optical switch stays on this optimal delay path to enable a continuous data transmission until the compensator enters the next training period.

It is well-known that in a digital transmission system, minimizing bit error rate (BER) is the final goal. This study adopts EOP as the performance criterion because EOP has high correlation to BER but takes much less integration time than BER does [25]. The EOP P is given by [12]

$$P = 10log_{10} \left[\frac{y_{min}(d=1) - y_{max}(d=0)}{y_{ideal}(d=1) - y_{ideal}(d=0)} \right], \tag{3.1}$$

where y represents the output of the photodetector at the receiver, and d denotes the input data bit. $y_{min}(d=1)$ refers to the minimum received optical power for bit "1" and $y_{max}(d=0)$ refers to the maximum received power for bit "0". $y_{ideal}(d=1)$ and $y_{ideal}(d=0)$ represent the received power for "1" and "0", respectively, in the absence of PMD.

An important practical question in designing the discretely tunable FOPMDC is how many delay paths are needed to cover a reasonable DGD dynamic range. Let the delay time increment (DTI) denote the delay difference generated by two successive parallel delay paths. Note that although DTI can be different from path to path, we use a fixed DTI in this study for simplicity. Hence a DTI of b ps implies that for a DGD range of $0 - B$ ps, $n = \lceil B/b \rceil$ paths, besides the one with zero delay, are required. The $\lceil \cdot \rceil$ denotes the rounding operation. It is

clear that for a fixed DGD coverage, a small DTI provides good tunability but requires a large number of delay paths. On the other hand, a large DTI enables the use of fewer delay paths but may have limited flexibility. Numerical results presented in next section demonstrate that the performance of the new scheme, as a function of b, approaches a limit rapidly as b decreases. And for DGD with a dynamic range of 5-116 ps, $b = 25$ ps is a good choice. Note that the limit represents the best performance that an ideal FOPMDC can achieve.

How often the pilot signal needs to be transmitted is determined by the prior information of the PMD dynamics. Since PMD changes slowly, on time scales of minutes in general, the pilot signal can be transmitted with low duty cycle. Consequently the overhead is expected to be negligible.

3.5   Simulation Results and Discussion

In this section, the proposed scheme is numerically simulated for NRZ 10 Gbit/s transmission over a virtual fiber link which has an average DGD of 32.5 ps and a DGD dynamic range of $4.7 - 78$ ps. The pilot signal, a 2^7-bit PRBS, is inserted in the data flow once every 1 s. The input signal is launched with its power equally distributed along the two input PSP's. Different DTI's, T, $T/2$, $T/4$, $T/8$, $T/16$, and $T/32$, are applied. T is 100 ps in the current 10 Gbit/s system. The simulated PMD-free SNR is adjusted to obtain a BER of 10^{-9}.

Fig. 3.3 demonstrates the time-varying fiber DGD as well as the optimal delay adjustments under three different DTI's. It is easy to see that under a DTI of $T/32$ (dot line), the optimal delay adjustments is superimposed on the time-varying fiber DGD to a certain degree. Fig. 3.4 summarizes the complementary cumulative distribution function (CDF) of the eye-opening penalty by using all
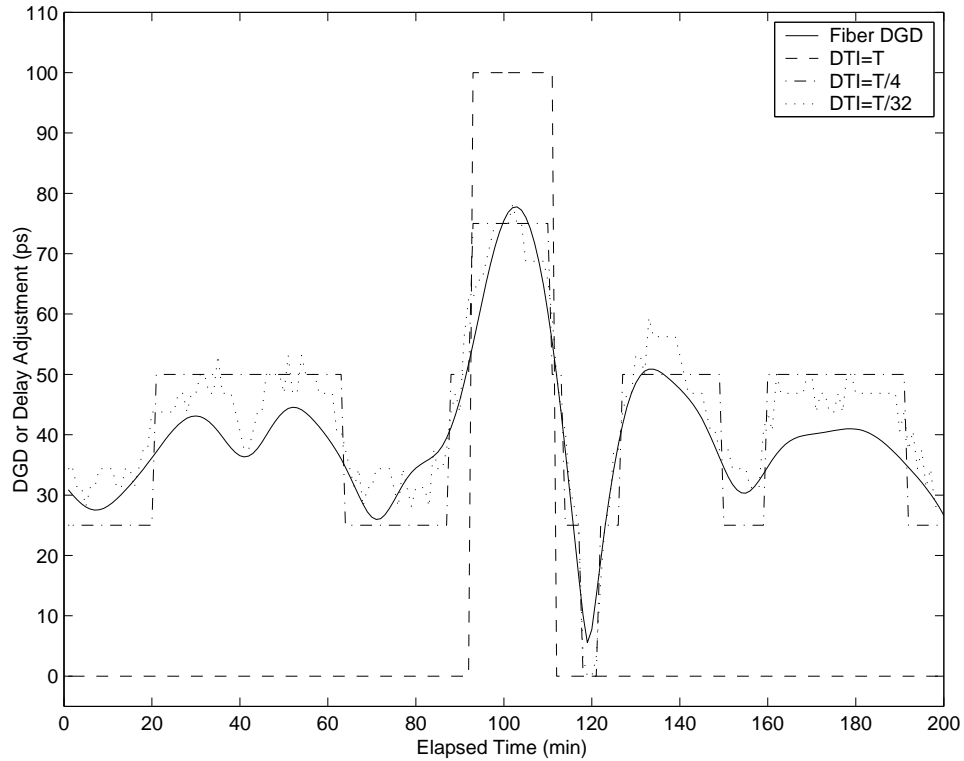
Figure 3.3: Comparison of fiber DGD and optimal delay adjustments under different DTI's.

aforementioned different DTI's. While a DTI of $T/4$ results in significant PMD mitigation, a smaller DTI can generate little further performance improvement. This indicates that $T/4$ (or 25 ps) is the best tradeoff between performance and complexity. This DTI is also verified to be good for another virtual fiber that has an average DGD of 58.7 ps and a dynamic range of $11 - 116$ ps.

The above feasibility of discrete tuning can be further supported by Fig. 3.5 in which the eye-opening penalty vs. delay adjustments is shown for 20 DGD samples in a continuous period of 20 minutes. As it illustrates, the curve of penalty vs. delay adjustments for each DGD sample has a relatively flat bottom. That is, the penalty is not sensitive to the delay adjustment once it is close
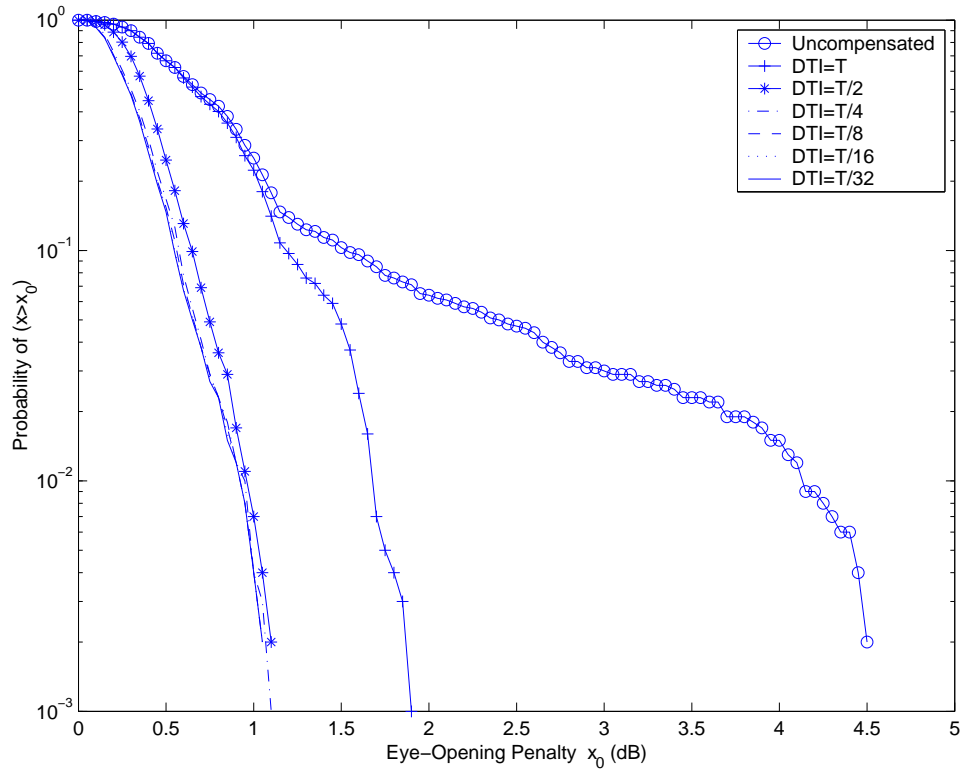
Figure 3.4: Complementary cumulative distribution function (CDF) of eye-opening penalty.

to the minimum. Therefore the optimal adjustment for one moment could be also good for the neighboring moments unless the PMD changes very fast. In the demonstrated case, a delay adjustment of 50 ps works well for the whole 20 minutes.

3.6 Conclusion

A low-complexity discretely tunable FOPMDC is presented along with discussion on the design of the delay line and numerical quantification of its performance. At a cost of negligible overhead, the new scheme achieves good PMD suppression.
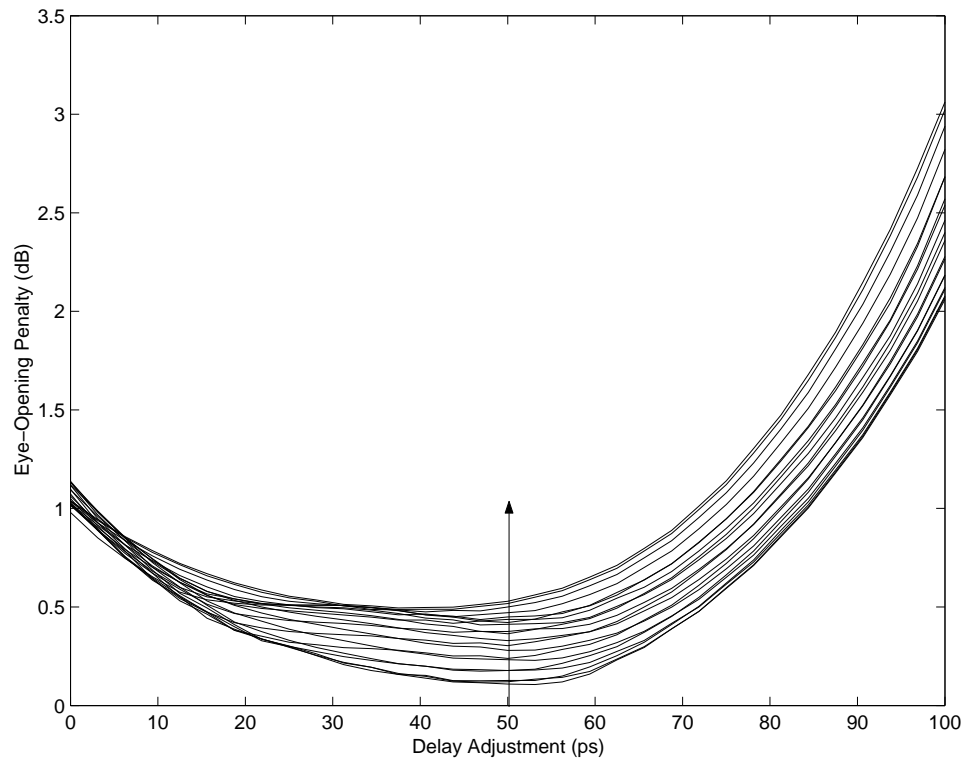
Figure 3.5: Eye-opening penalty vs. delay adjustments.

CHAPTER 4

Peak-to-Average Power Ratio Reduction for OFDM

4.1 Introduction

In the last few years orthogonal frequency division multiplexing (OFDM) has attracted increased research interest due to its high spectral efficiency and robustness to multipath fading [41]. It has been adopted for several types of high-data-rate wireless communication systems, including Digital Video Broadcasting [42], HYPERLAN-II [43], and wireless local area networking (WLAN).

Performance of OFDM, however, is seriously limited by imperfect synchronization and the high peak-to-average power ratio (PAR) of the transmitted signal. The impact of frequency offset and timing error along with a comparison of frequency offset estimation methods will be presented in Chapter 5. The current chapter is focused on the PAR reduction. After a brief overview of existing strategies for the purpose, a new scheme is proposed.

OFDM modulation combats the multipath fading by splitting the incoming data stream into several parallel streams of lower rate, and transmitting each of them in a different narrowband subchannel. Due to the large number of subchannels, the peak of an OFDM signal with N subcarriers could reach N times that of a single carrier system with the same power. In order to avoid nonlinear dis-

tortion when power amplifiers are used, expensive high-power amplifiers (HPA) are required. However, the power consumption of a HPA depends largely on its peak power output, and thus dealing with occasional large peaks leads to low power efficiency. This low power efficiency is undesirable for a mobile or portable transmitter where energy is a limited resource.

In order to transmit OFDM signals with good spectral and power efficiency, research efforts have been actively made in two directions, either linearizing the power amplifier or reducing the peak-to-average power ratio. Techniques for power amplifier linearization include power backoff, corrective distortion [27], and envelop elimination and restoration [28]. Each of these approaches has its own advantages and design concerns. Methods for minimizing the PAR of the signal waveform include Clipping and Filtering [57], Complementary Golay Sequences [30], Tone Reservation [35], Selected Mapping [31], and Partial Transmit Sequences [32].

Clipping results in serious out-of-band radiation and in-band noise. To reduce the out-of-band emission, filtering after clipping is required, which may induce spectral regrowth and decrease the bandwidth efficiency.

In [30], information is transmitted by mapping each data word into a Golay sequence which has a limited PAR between 3 and 6 dB. Since the code rate is shown to decrease exponentially as code length increases, this method is not feasible for systems with a large number of subcarriers ($>$1024).

Tellado et al. proposed exploiting reserved or unused (due to low SNR) tones to lower the PAR of a transmitted data block [35]. Krongold et al. extended the technique to both the real-baseband and complex-baseband cases [36]. Such solutions usually reduce bandwidth efficiency of the system to a certain degree.

Selected mapping generates a large set of data vectors representing the same

information [31]. The data vector with the lowest PAR is then selected. Information about which particular data vector was used is sent as side information. This method results in significant PAR reduction even at low redundancy. However, the side information needs to be specially protected.

The scheme of partial transmit sequences (PTS) results in significant PAR improvement at low redundancy, and no distortion is introduced. Just as Selected Mapping, it requires transmission of side information. A comparison between PTS and Slected Mapping is presented in [38] with the conclusion that the former is slightly better due to its lower complexity. However, in order to achieve the best performance, PTS requires exhaustive search in the parameter space. In [34], an alternative PTS algorithm, referred to as iterative PTS or IPTS, is presented that achieves good performance at reduced complexity.

In this chapter, after briefing the OFDM modulation and the PAR properties of OFDM signals, we revisit the general PTS scheme, give a geometrical interpretation to combining in any PTS approach, and introduce a novel orthogonal projection-based PTS (OPPTS) method for PAR reduction. The computational complexity as well as performance of the proposed method are evaluated and compared with exhaustive search in [33] and IPTS in [34].

4.2   PAR Properties of OFDM Signals

In an OFDM system with N subchannels, the complex baseband representation of an OFDM signal is given by [37]

$$h(t) = \frac{1}{\sqrt{N}} \sum_{n=0}^{N-1} m_n \cdot e^{jn\Delta wt}, 0 \le t < NT, \tag{4.1}$$

where Δw is the frequency spacing, m_n is the transmitted symbol at Subchannel n, and T is the original symbol period.

The PAR is defined as the squared maximum magnitude of a time-continuous OFDM symbol divided by the ensemble rms value, that is,

$$PAR = \frac{\max_{t\in[0,NT)}\{|h(t)|^2\}}{P_{av}}, \tag{4.2}$$

with

$$P_{av} = E\{\frac{1}{NT}\int_{t=0}^{NT}|h(t)|^2dt\}.$$

Fig. 4.1 depicts the complementary cumulative distribution of PAR for various values of N and constellation size M. Clearly, the PAR increase with the number of subchannels. In the meanwhile, for a fixed number of subchannels, the
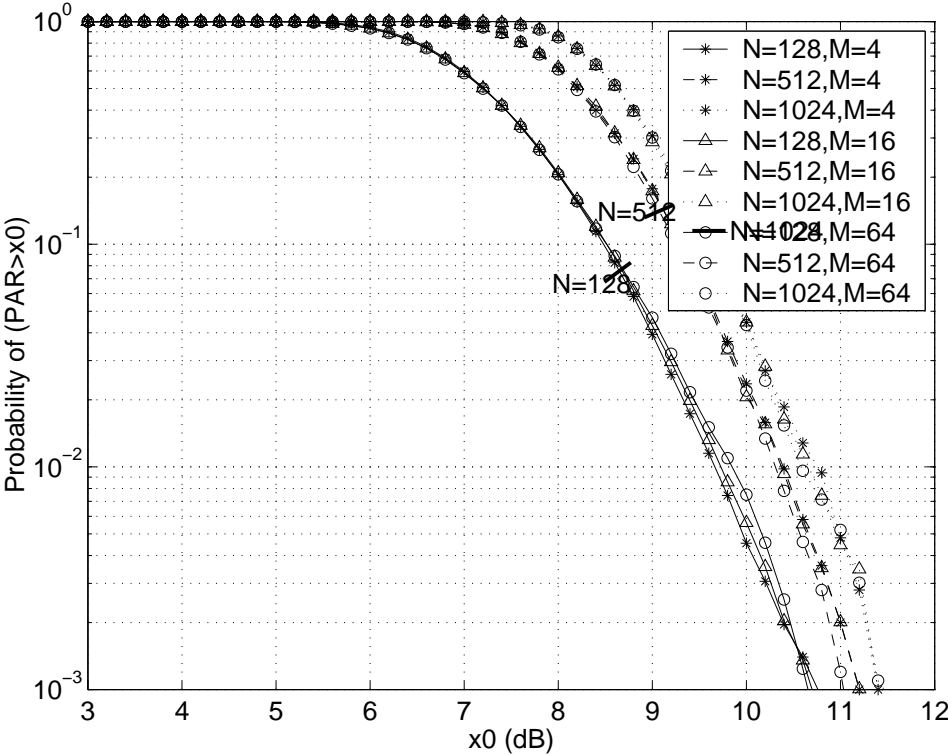
Figure 4.1: Complementary cumulative distribution of peak-to-average power ratio. N stands for the number of subchannel, and M the constellation size. The RMS value of all the signals was normalized to unity.

statistical behavior of the PAR is almost independent of modulation scheme.

4.3 Partial Transmit Sequences

The principle of PTS is described as follows. First, an OFDM symbol in the frequency domain, $S = [\ m_1 \quad m_2 \quad \cdots \quad m_N\ ]$, is partitioned into V pairwise disjoint subblocks $S^{(v)}, 1 \leq v \leq V$, and each is multiplied by a constant complex-valued phase factor b_v, $b_v = e^{j\phi_v}, \phi_v \in [0, 2\pi), 1 \leq v \leq V$. The OFDM symbol is therefore modified to

$$S = \sum_{v=1}^{V} b_v S^{(v)}. \tag{4.3}$$

Next, the OFDM symbol in the time domain is found by applying the inverse DFT to both sides of Equation (4.3),

$$s = IDFT\{S\} = \sum_{v=1}^{V} b_v IDFT\{S^{(v)}\} = \sum_{v=1}^{V} b_v s_v. \tag{4.4}$$

Here $s_v, 1 \leq v \leq V$, are called partial transmit sequences, which explains the name of the scheme. To minimize the PAR, the free parameters $b_v, 1 \leq v \leq V$, are properly chosen from a finite set of W allowed phase angles. In the literature, $W = 4$ has been shown to be a good choice since a larger W results in negligible gain. The optimum phase factors for the OFDM symbol are then given by

$$\{b_1^*, \cdots, b_V^*\} = arg \min_{\{b_1, \cdots, b_V\}} \left(\max \left| \sum_{v=1}^{V} b_v s_v \right| \right). \tag{4.5}$$

It is easy to see that $Nlog_2 M$ is the total number of bits transmitted in an OFDM symbol, and $(V-1)log_2 W$ is the number of bits required for representing the phase vector. The introduced redundancy is therefore $R = (V - 1)log_2 W/(Nlog_2 M)$.

4.4 Proposed Scheme: Orthogonal Projection-Based PTS

Define A to be the $V \times N$ matrix whose vth row is s_v in Equation (4.4). s can be rewritten as

$$s = \sum_{v=1}^{V} b_v s_v = b^T A = [\ b^T a_1 \quad b^T a_2 \quad \cdots \quad b^T a_N\ ], \tag{4.6}$$

where a_n denotes the nth column of Matrix A, and b is a column phase vector of length V, $b = [\ b_1 \quad b_2 \quad \cdots \quad b_V\ ]^T$. It can be seen that the aim of the PTS scheme is actually to minimize $\|b^T A\|_\infty$, or the maximum magnitude of $b^T a_n, 1 \le n \le N$. Since the inner product $b^T a_n$ is proportional to the projection of Vector b onto Vector a_n, a desired phase vector b in the PTS scheme is revealed to be the one that results in small projections onto all vectors $a_n, 1 \le n \le N$. This geometrical interpretation to proper combining motivated us to find a good phase vector b based on the orthogonal vectors y_n of the columns $a_n, 1 \le n \le N$. The details are described as follows.

First, find y_n by projecting a pre-chosen vector (for example, an all-ones vector 1) onto the null-space of a_n, that is,

$$y_n = (I - a_n(a_n^T a_n)^{-1}a_n^T)1 = 1 - a_n(a_n^T 1)/(a_n^T a_n). \tag{4.7}$$

It is obvious $|y_n^T a_n| = 0$. To get a phase vector candidate x_n, modify each element of y_n to the closest phase in the allowed phase angles set. The resulting $|x_n^T a_n|$ is a small number. However, $|x_n^T a_j|$ can be large when $j \ne n$. Next, calculate the PAR resulting from x_n by evaluating $\|x_n^T A\|_\infty$. Fig. 4.2 shows the PARs resulting from all phase vector candidates $x_n, 1 \le n \le N$, for a randomly generated OFDM symbol. Finally, choose x_n that provides the lowest PAR to be the proper phase vector for the current OFDM symbol. Note that any phase vector can be simply rotated to have $b_1 = 1$.
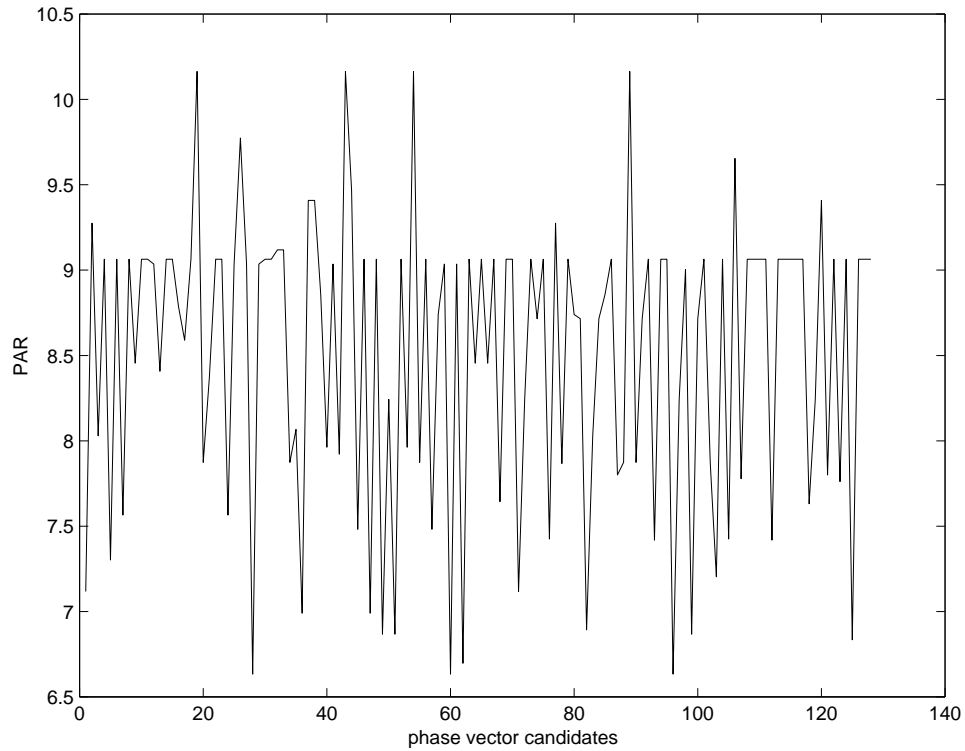
Figure 4.2: PAR vs. phase vector candidates.

Compared to W^{V-1} trials required by exhaustive search [33] and $(V-1)W$ trials by the iterative PTS [34], OPPTS requires N trials plus NV complex multiplications. For small N, W and V, such as $N = 128, W = 4$ and $V \leq 5$, exhaustive search always wins OPPTS. However, when N and V are reasonably large, for example, $N = 1024, V = 32, W = 4$, OPPTS saves a significant amount of computation by needing only 2^{15} complex multiplications plus 2^{10} trials while exhaustive search requires 2^{62} trials. In fact, the computational complexity of OPPTS can be further reduced. Fig. 4.2 shows that there is more than one phase vector candidate achieving a sufficiently low PAR, and the first one could occur within the first few candidates. Thus a better way, named partial search, is to adopt the best phase vector among the first U $(U < N)$ candidates. Fig. 4.3

shows the complementary cumulative distribution function (CDF) of the PAR using OPPTS with different U at two redundancy levels, $R = 1.2\%$ and $R = 2.3\%$, respectively. It can be seen that this alternative can reduce the total number of trials and complex multiplications by at least 50%, without hurting the performance.
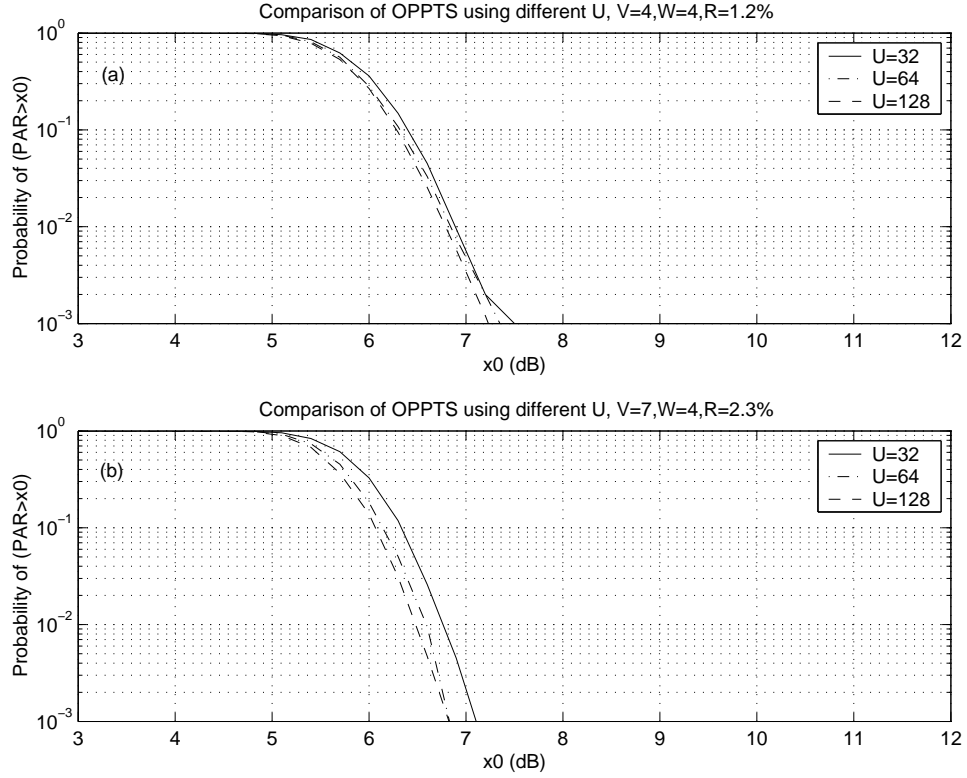
Figure 4.3: Performance comparison of partial search and full search in OPPTS. Two cases are considered. Part (a): $R = 1.2\%$; Part (b): $R = 2.3\%$.

4.5   Simulation Results and Discussion

The simulation environment is an OFDM system with 128 subchannels (if not specified) and 16-QAM modulation over all subchannels. Adjacent partitioning

and partial search with $U = N/2$ are used in all simulations.
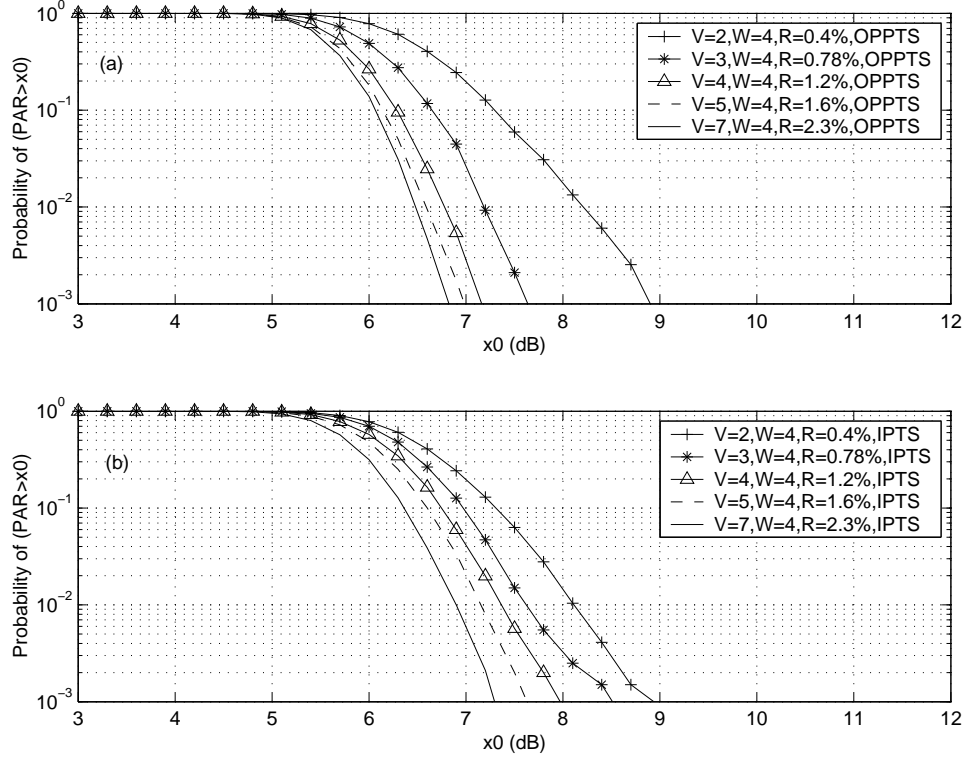
Figure 4.4: Performance comparison of OPPTS and IPTS. Part (a): Performance of OPPTS; Part (b): Performance of IPTS.

Part (a) of Fig. 4.4 shows the performance of OPPTS at different levels of redundancy. The original OFDM signal has a PAR that exceeds 10.6 dB for less than 0.1% of the signals. Using OPPTS, the 0.1% PAR reduces to 8.9 dB at a redundancy of 0.4%, and to 6.9 dB at 1.6% redundancy. At low redundancy, excluding the 2-subblock case where three aforementioned approaches achieve the same performance, OPPTS shows only $0.4 - 0.8$ dB degradation from the best possible exhaustive search results in [38] where the simple adjacent partitioning has already been replaced with pseudo-random partitioning for achieving better performance. Our approach also outperforms the iterative PTS (its performance

47

is shown in Part (b) of Fig. 4.4) by $0.4 - 0.7$ dB. To confirm the performance of our approach in OFDM systems with more subcarriers, Fig. 4.5 shows that a PAR reduction of $3.7 - 3.9$ dB can be achieved at a redundancy of 2% for N=128, 512, and 1024.
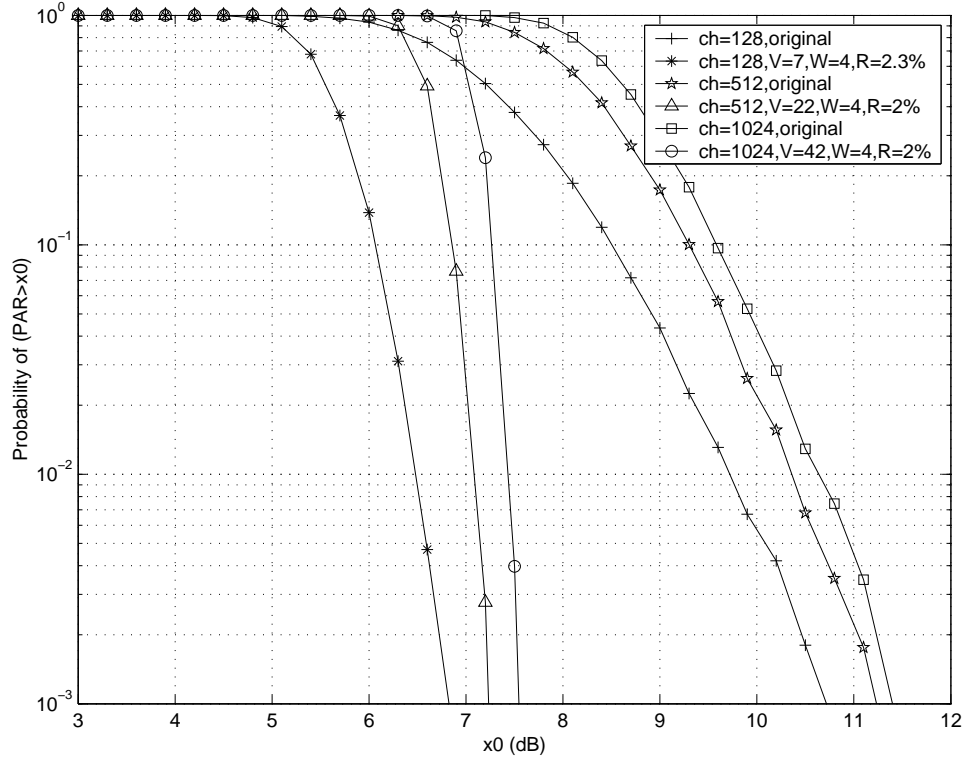
Figure 4.5: Performance of OPPTS in OFDM systems with various numbers of subchannels.

For a fixed N, while partitioning the subchannels into a large number of subblocks which implies high redundancy, we observed that the further improvement from using OPPTS becomes small. This is because with more subblocks, the columns in A become more independent from each other and the flexibility to get a "common" near-orthogonal vector decreases. This limits the usefulness of OPPTS when high redundancy is allowed.

Certainly the receiver should be informed of the phase vector so that it can undo the combining to get the original OFDM symbol back. An easy way, subject to certain performance loss, is to allocate information bits onto the first $N - Q$ subchannels (leave the rest Q subchannels in arbitrary states), then find the best possible phase vector and put the side-information onto the last Q subchannels. For a relatively small Q compared to N, for example, $\frac{Q}{N} \leq \frac{1}{32}$ which corresponds to a redundancy up to 3%, our simulations show that the performance loss is within 1 dB. When the side-information is required to be specially protected, the overhead will be bigger than what we show here.

Also, in the literature, two careful designs are often considered in a PTS scheme to improve its performance. The first strategy is to oversample the OFDM signal to catch the hidden peak. In our approach, this modification simply means replacing all length-N DFT/IDFTs with length-$\hat{N}$ ($\hat{N} > N$) DFT/IDFTs. In consequence Matrix A will have $\hat{N}$ instead of N columns. The second strategy is, as mentioned before, to replace adjacent partitioning with pseudo-random partitioning. Again, this just implies a different way for constructing Matrix A. Since the orthogonal-projecting operation in OPPTS is independent of the formulation of Matrix A, our approach can be easily extended to include these two designs. However using pseudo-random partitioning implies that more side-information needs to be transmitted to the receiver, which complicates the detection process.

4.6 Conclusion

We presented an orthogonal projection-based PTS method for PAR reduction in OFDM systems. Simulation results showed that at low redundancy the proposed scheme experiences only $0.4 - 0.8$ dB degradation from the best possible exhaustive search results. This study also for the first time provided geometrical

interpretation to combining in the well-known partial transmit sequences scheme.

CHAPTER 5

Frequency Synchronization for OFDM

5.1   Introduction

Performance of OFDM is highly sensitive to imperfect synchronization. In particular, the carrier frequency offset causes a number of impairments including attenuation/rotation of received OFDM symbols and intercarrier interference (ICI), which degrade the BER of the system [44, 58]. To overcome this sensitivity to frequency offset, various methods for frequency synchronization have been proposed [58]-[46].

The synchronization process is normally split into an acquisition phase and a tracking phase, in order to minimize both the overhead and the computational effort at the receiver [46]. In the acquisition phase, a coarse estimate of the errors is made. The residual small deviations are then corrected in the tracking mode. For the subsequent frequency tracking algorithms to operate reliably, the initial estimate is required to be accurate to half a subcarrier spacing. The focus of this chapter is the frequency offset tracking problem.

The algorithms that are already available for frequency offset tracking can be classified into three categories, i.e., pilot tone-aided (PTA), cyclic prefix-based (CPB), and decision-directed (DD) schemes. PTA approaches estimate frequency offsets by periodically inserting pilots on particular subacrriers and correlating the received symbols with known symbols. CPB methods are generally based on

correlating received samples taken one OFDM data block length apart, utilizing the periodicity created by the insertion of the cyclic prefix (CP). DD schemes are in principle identical to PTA approaches, except that tentative decisions replace known symbols. Note that in general DD algorithms are not recommended as their performance is often degraded by delay and possible error propagation.

The principles of PTA and CPB methods have been presented in the literature, e.g., [59, 46]. For all the CPB estimators, a unified structure was also proposed [47]. However, to our knowledge, a direct and complete comparison of PTA and CPB schemes has not been reported to date. It is the aim of this chapter to evaluate the two methods in the same environment and compare their sensitivities to frequency offset, constellation size, and timing error. This comparison helps in determining the most suitable frequency offset tracking scheme for a particular application under consideration.

The rest of this chapter is organized as follows. Section 5.2 presents the system model. Section 5.3 briefly revisits the principles of PTA and CPB methods. Two modifications we found necessary are proposed for the algorithms. Section 5.4 presents simulation results. Section 5.5 concludes the chapter.

5.2   System Model

We assume a finite channel impulse response with L samples, $h = [h_1, ..., h_L]^T$. At the transmitter, the kth sample of an OFDM block generated by the Inverse Fast Fourier Transform (IFFT) is

$$x_k = \sqrt{\frac{1}{N}} \sum_{n=0}^{N-1} X_n e^{j2\pi \frac{kn}{N}}, 0 \le k \le N - 1. \tag{5.1}$$

Here X_n is the data symbol modulated onto the nth subcarrier, and N is the number of subcarriers. After the data are converted into a sequence in the time

domain, a cyclic prefix of length N_g $(N_g > L)$ is added. Thus the actual transmitted OFDM block is

$$\bar{x} = [x_{N-N_g}, ..., x_{N-1}, x_0, ..., x_{N-1}]^T.$$

The received sequence is the convolution of the transmitted sequence with the channel impulse response, i.e.,

$$\bar{r} = \bar{x} * h. \tag{5.2}$$

When a frequency offset exists, the received OFDM signal is

$$z_k = r_k e^{j2\pi\delta_f k/N} + \omega_k, \tag{5.3}$$

where $\delta_f = \frac{\epsilon}{\Delta f}$ is the relative frequency offset of the channel (the ratio of the actual frequency offset ϵ to the subcarrier spacing Δf), and ω is the additive white Gaussian noise (AWGN). Both data and noise sequences are assumed to be uncorrelated, independent and identically distributed (i.i.d.) random variables with power of σ_s^2 and σ_n^2, respectively. At the receiver, samples corresponding to the cyclic prefix are removed and the remaining N samples are used for demodulation. After the FFT operation, the symbol on the nth subcarrier is

$$Z_n = \sqrt{\frac{1}{N}} \sum_{k=0}^{N-1} z_k e^{-j2\pi\frac{kn}{N}}, 0 \leq n \leq N - 1. \tag{5.4}$$

Previous studies have shown that both the cyclic prefix and pilot tones can be used to track frequency offset. In the next section we review these two approaches and make necessary modifications to the algorithms. In order to separate the effects of frequency offset from other degradations, frame and symbol timing are assumed to be perfect unless otherwise specified, and the channel is assumed to be slow-fading. Throughout this chapter, the signal-to-noise ratio (SNR) is defined as SNR $= \sigma_s^2/\sigma_n^2$.
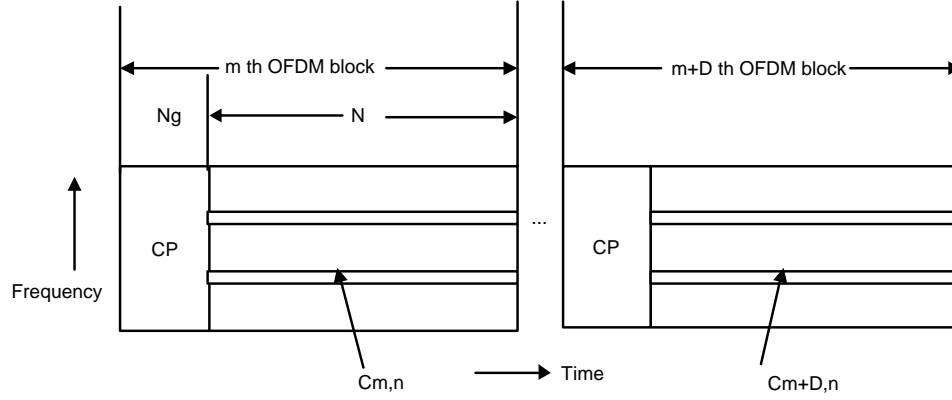
Figure 5.1: Reference OFDM blocks, CP stands for cyclic prefix.

5.3 Frequency Offset Tracking Algorithms

5.3.1 Pilot Tone-Aided Frequency Offset Tracking

Assume that one transmitted OFDM block consists of N subcarriers. Among them, N_p subcarriers are modulated by pilot symbols. Let P denote the set of indexes of the N_p pilot carriers. A pilot tone-aided method has the following structure [59]

$$\frac{N + N_g}{N} \cdot D \cdot \delta_f =$$

$$\frac{1}{2\pi} \cdot arg\{\sum_{n \in P} \left(Z_{m,n} Z^*_{m+D,n}\right) (C^*_{m,n} C_{m+D,n})\}. \tag{5.5}$$

Here m and $m+D$ respectively represent the mth and $(m+D)^{th}$ OFDM blocks, as shown in Fig. 5.1. $\{C_{m,n}\}$ and $\{C_{m+D,n}\}$ are pilot symbols transmitted over the same n^{th} subchannel during the mth and $(m+D)^{th}$ time period, respectively. $Z_{m,n}$ and $Z_{m+D,n}$ are the symbols received over the nth subchannel in the two periods. D is an integer which indicates that $D - 1$ other OFDM blocks can be placed between a pair of pilot symbol-embedded OFDM blocks. The multiplication

with the conjugate complex value of the transmitted symbols serves to remove the influence of the modulation. Note that the original algorithm in [59] does not have the term $\frac{N+N_g}{N}$ at the left side of (5.5). We found the correction is necessary because according to (5.3), the phase difference between $z_{m,k}$ and $z_{m+D,k}$ is $(N + N_g)D/N$ which can be reduced to D only if $N >> N_g$.

Since the PTA scheme involves the demodulation process which is implemented with a Discrete Fourier Transform (DFT), it is inevitably subject to ICI. The bound of the frequency offset-induced ICI was derived by Moose [58]. To brief the bound here, we rewrite (5.3) into

$$z_k = \sqrt{\frac{1}{N}} \left[\sum_{n=0}^{N-1} X_n H_n e^{j2\pi k(n+\delta_f)/N} \right] + \omega_k, 0 \leq k \leq N - 1, \quad (5.6)$$

where H_n is the transfer function of the channel at the frequency of the nth carrier. The nth element of the DFT sequence Z_n shown in (5.4) can be decomposed into three components

$$Z_n = (X_n H_n) \cdot \frac{\sin(\pi \delta_f)}{N \sin(\pi \delta_f/N)} \cdot e^{j\pi \delta_f(N-1)/N} + I_n + W_n. \quad (5.7)$$

The first component is the OFDM symbol X_n modified by the channel transfer function. This component experiences an amplitude reduction and phase shift due to the frequency offset. The second term is the ICI caused by the frequency offset and is given by

$$I_n = \sum_{l=0,l\neq n}^{N-1} (X_l H_l) \frac{\sin(\pi \delta_f)}{N \sin(\pi(l - n + \delta_f)/N)}$$

$$\cdot e^{j\pi \delta_f(N-1)/N} \cdot e^{-j\pi(l-n)/N}. \quad (5.8)$$

Assuming that the data have zero mean and are uncorrelated, Moose showed that $E\{I_n\} = 0$, and

$$E|I_n|^2 \leq 0.5947|X|^2|H|^2 \sin^2(\pi \delta_f), |\delta_f| \leq 0.5. \quad (5.9)$$

55
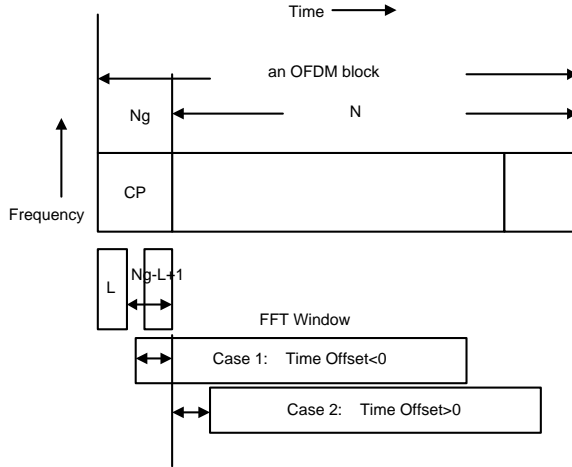
Figure 5.2: Reference plot for cyclic prefix-based method and imperfect timing synchronization.

Clearly, I_n is proportional to frequency offset, and the system tolerance to noise decreases as the constellation size increases. Therefore, PTA schemes degrade with the increase of the frequency offset δ_f and/or constellation size M.

5.3.2 Cyclic Prefix-Based Frequency Offset Tracking

As implied by (5.3), a carrier frequency error of δ_f results in an evolving phase error $p(k)$ in the received samples $z(k)$,

$$p(k) = \frac{2\pi\delta_f k}{N}. \tag{5.10}$$

Therefore, the phase error difference between two samples $z(k_1)$ and $z(k_2)$ is a function of the frequency error and their time difference. When the original phase difference between $z(k_1)$ and $z(k_2)$ is known and all other phase distortion is absent, the relative frequency error δ_f can be derived from the phase error difference.

The time-domain samples of the cyclic extension are a copy of the last N_g data

samples of the OFDM block. As shown in Fig. 5.2, after the OFDM block passes through a channel of length L, $N_g - L + 1$ pairs of samples in the received signal remain identical except for a phase difference of $2\pi\delta_f$. Clearly the frequency error can be estimated using each of these $N_g - L + 1$ pairs of samples. To improve the estimation accuracy when exposed to noise and other channel impairments, averaging should be carried out over the $N_g - L + 1$ estimates.

Note that in the literature the whole cyclic prefix of N_g samples are often used for averaging. However, we noticed that the first $L - 1$ samples in the received OFDM block are usually corrupted by interference from the previous OFDM block. To show that $N_g - L + 1$ instead of N_g samples should be used for reliable frequency offset tracking when all subcarriers are modulated with data symbols, Fig. 5.3 compares the two different choices in terms of mean square error in the estimate. For zero frequency offset and SNR of 15 dB, the MSE is improved from 10^{-3} to 10^{-4} by replacing N_g with $N_g - L + 1$. The gain from averaging over $N_g - L + 1$ samples becomes even more significant as SNR increases.

The above frequency offset tracking algorithm relies on the evaluation of the following correlation function

$$p(k) = \sum_{m=0}^{N_g - L} z(k - m) \cdot z(k - m - N)^* \qquad (5.11)$$

where k is the index of the most recent input sample. When the timing is correct, a correlation peak indicated by $p(k_{\max})$ can be achieved, and the phase of $p(k_{\max})$ equals the averaged phase shift between the guard time samples and the corresponding data samples of the current OFDM block. Since the sample pairs are spaced by N samples, this leads to the fine frequency offset estimation given by

$$\delta_f = \frac{p(k_{\max})}{2\pi}. \qquad (5.12)$$
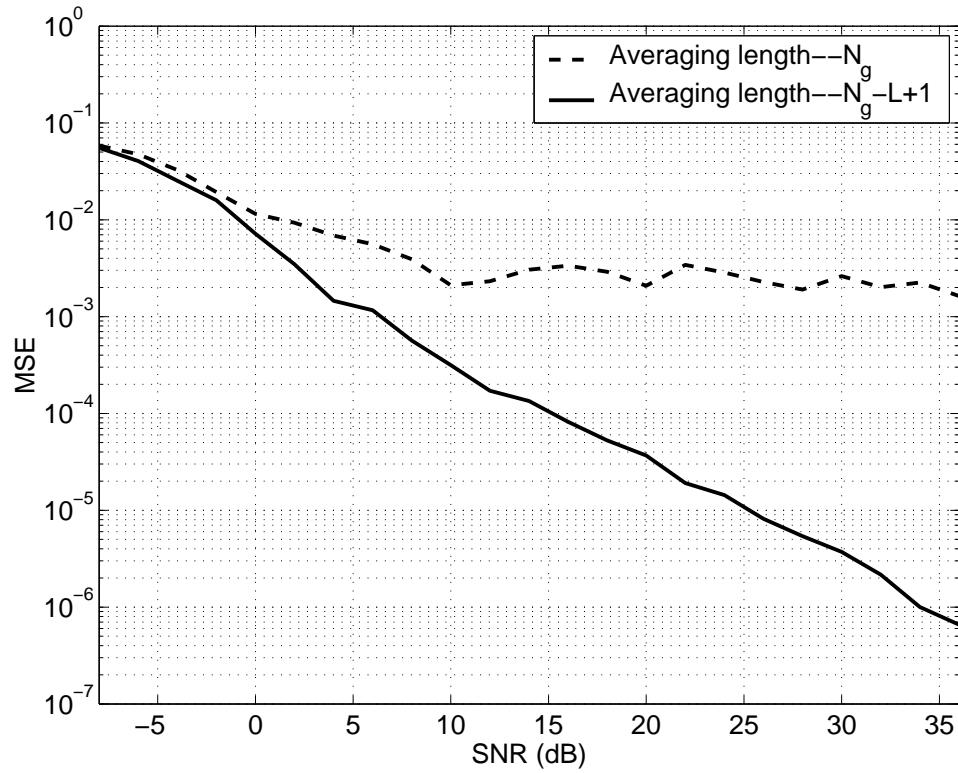
Figure 5.3: Performance comparison of the traditional CPB method using N_g samples and the new CPB method using $N_g - L + 1$ samples. $N_g = 16, L = 8$. Frequency offset is set to 0.

Here the 2π ambiguity of the phase once again implies that a tracking algorithm can only handle frequency errors smaller than $\Delta f/2$.

5.4 Comparison of Frequency Offset Tracking Algorithms in Simulation

To make a fair comparison, the same overhead is used for both algorithms. In other words, the number of pilot tones plus the number of cyclic prefix samples in the PTA algorithm equals the number of cyclic prefix samples in the CPB algorithm. The mean square error (MSE) in the estimate is evaluated for various frequency offsets, $\delta_f = 0, 0.1, 0.2$, and different constellation sizes, $M = 4, 16, 64$. All simulations were run for 10000 OFDM blocks to provide results showing statistical information.

5.4.1 Simulation Environment

The number of subcarriers is fixed at 128. The length of the cyclic prefix is set at 8 for the PTA algorithm and 16 for the CPB algorithm. The number of pilot tones for PTA equals 8. Also, a frequency-selective channel is simulated with the following parameters: 1) the length of the channel corresponds to L=8; 2) the channel delay spread equals 70 ns; and 3) the sampling period is T_s=50 ns. The channel model we adopted here was developed by the PCS Joint Technical Committee (JTC) for simulation of radio propagation for Indoor Office environment [48]. The model uses a series of weighted delay taps to simulate multipath propagation. Each tap weight is a Rayleigh distributed random variable with average relative amplitude as shown in Table 5.1. The phase of each tap is a uniformly distributed random variable in $[0, 2\pi)$.

Table 5.1: The average relative amplitudes of the channel tap weights

Tap	Delay (nsec)	Relative Amplitude (dB)
1	0	0
2	50	-2.9
3	100	-5.8
4	150	-8.7
5	200	-11.6
6	250	-14.5
7	300	-17.4
8	350	-20.3

5.4.2 Results and Discussion

5.4.2.1 Sensitivity to SNR, Frequency Offset, and Constellation Size

The performance of the described PTA scheme is shown in Fig. 5.4. Part a) illustrates the resulting MSE in the scenario of QAM signaling. As can be seen, without a frequency offset the MSE decreases as SNR increases. However, when a nonzero offset exists, an error floor is observed. This verifies the influence of the ICI analyzed in Section III. In addition, note that the error floor rises significantly as the frequency offset increases. It is not surprising because the frequency offset-induced ICI is proportional to the frequency offset. Parts b) and c) in Fig. 5.4 respectively demonstrate the obtained MSE for the cases of $16 - QAM$ and $64 - QAM$ signaling. Clearly, the PTA scheme behaves worse for higher order modulations due to its reduced tolerance to noise. Specifically, when $\delta_f = 0.0$, in order to keep MSE at the level of 10^{-3}, SNR needs to increase about 8 dB when using 16-QAM instead of QAM, and another 6 dB if 64-QAM

60
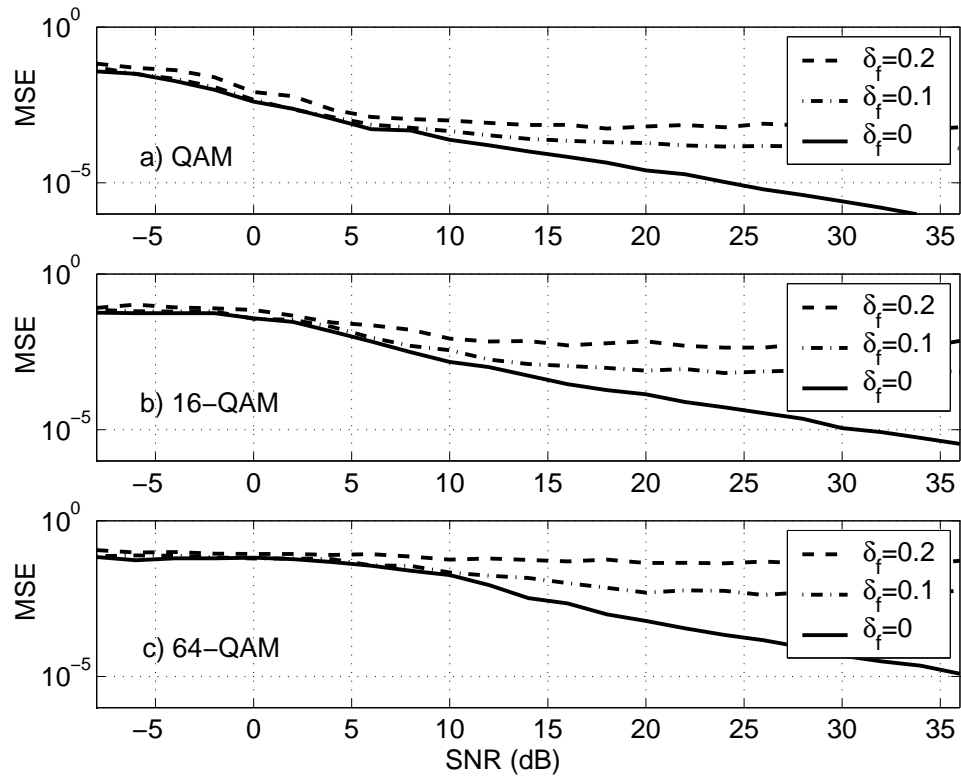
Figure 5.4: MSE performance of PTA for various levels of frequency offset and different constellation sizes. $N = 128, N_g = 8, N_p = 8, D = 1$.
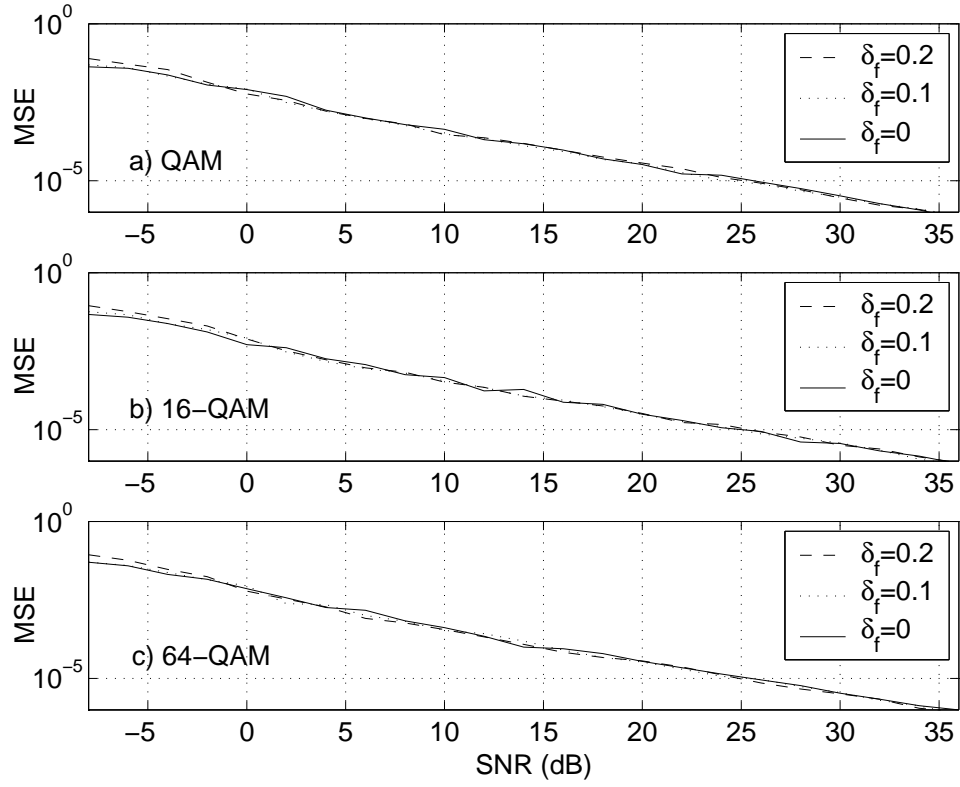
Figure 5.5: MSE performance of CPB for various levels of frequency offset and different constellation sizes. $N = 128, N_g = 16$.

is used.

Fig. 5.5 shows the performance of the CPB scheme. Again MSE in the estimate is evaluated for various frequency offsets and constellation sizes. We can see that for zero offset and QAM signaling, the MSE decreases with increasing SNR, just as in the PTA scheme. On the other hand, in this case the resulting MSE is very robust against the variation in the frequency offset and/or constellation size. Only at very low SNR (< 0 dB) does the resulting MSE consistently but negligibly rise as frequency offset increases.

To directly compare the above two approaches, Fig. 5.6 collects the simulation results for QAM signaling. It can be seen that with zero frequency offset, the
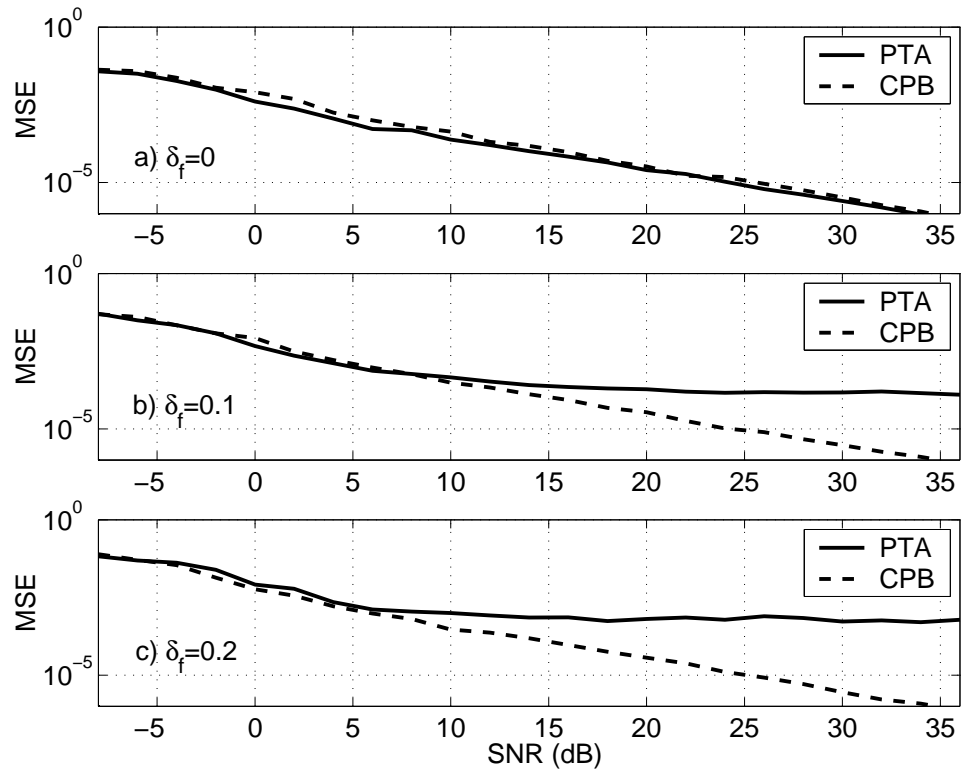
Figure 5.6: Direct comparison of PTA and CPB for QAM signaling at various levels of frequency offset.
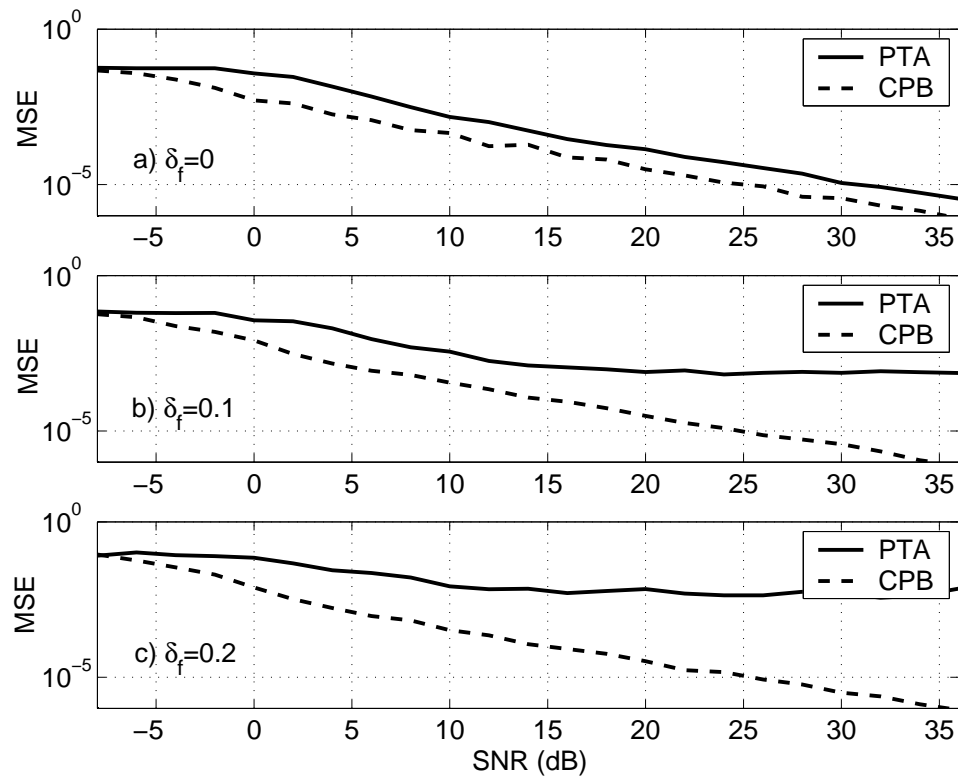
Figure 5.7: Direct comparison of PTA and CPB for 16-QAM signaling at various levels of frequency offset.

PTA scheme is slightly better than the CPB method at all SNR levels. However, with nonzero offsets, PTA is superior over CPB only at very low SNR. In Fig. 5.7 where the simulation results for 16-QAM signaling are summarized, we see that the CPB method is always better than the PTA scheme. The same property has been verified for the case of 64-QAM. Note that the demonstrated robustness of the CPB scheme against constellation size contradicts the conjecture in [59] that non-data-aided structures fail when high order modulation schemes are used.

5.4.2.2   Sensitivity to Timing Error

So far perfect time synchronization has been assumed, which is not true in real applications. To investigate the sensitivity of the above methods to timing errors, we introduced symbol offsets of -4, -2, 0, 2, and 4 samples respectively, then repeated the above simulations. Here a negative time offset means that the FFT window starts earlier than it should, as indicated in Fig. 5.2. In this case the beginning of the FFT window remains within the cyclic prefix, therefore the orthogonality of the carriers is maintained. A positive time offset, on the other hand, corresponds to a late start of the FFT window. Clearly, it degrades the FFT demodulation due to the loss of the beginning part of the OFDM data block. Fig. 5.8 illustrates the resulting MSE for both the PTA and CPB schemes. It is shown that the performance of the PTA scheme is very robust to negative time offsets and degrades in the presence of positive time offsets. However, the CPB scheme is sensitive to time offset in both directions. And overall, the PTA scheme is less sensitive to timing error than the CPB scheme.
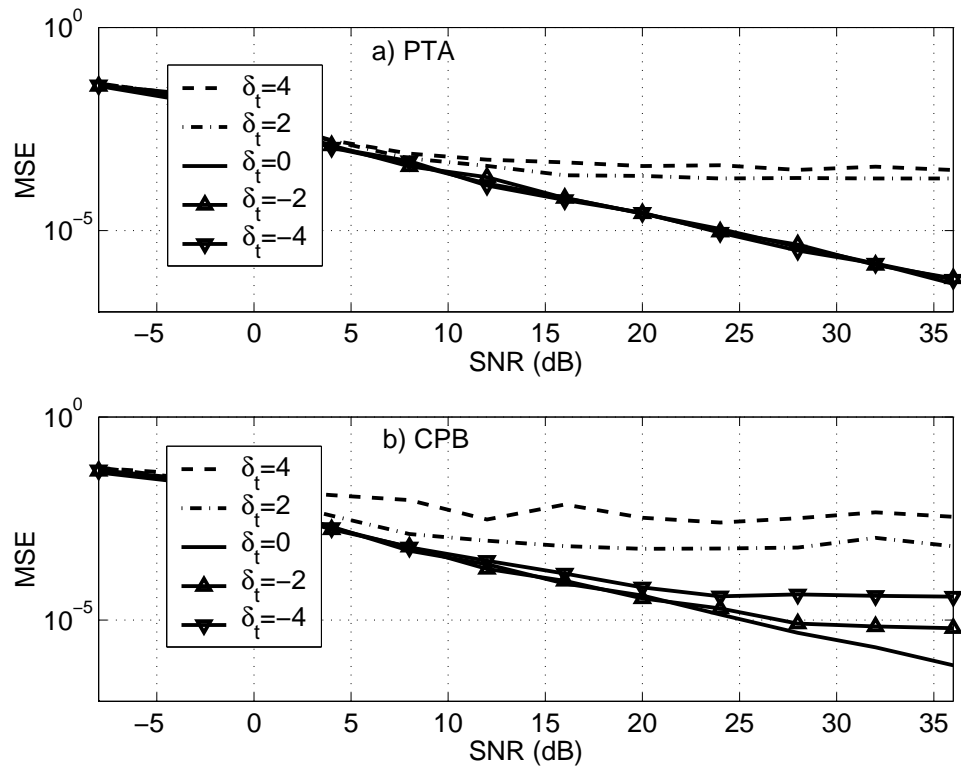
Figure 5.8: MSE versus SNR performance curves of PTA and CPB in the scenario of imperfect timing synchronization. Time offsets of 4,2,0,-2, and -4 samples, are considered. Perfect frequency synchronization is assumed, and QAM signaling is applied.

5.5 Conclusion

In this chapter we compared two popular candidates for frequency offset tracking in OFDM systems. Extensive simulations show that the pilot tone-based algorithm is sensitive to both frequency offset and modulation scheme, and the cyclic prefix-based method is sensitive to timing error. Since the PTA scheme also needs greater channel stability (it operates on at least two sequential OFDM blocks), we conclude that CPB is overall a better approach for frequency offset tracking.

Note that in our study, we have assumed that the CPB scheme does not need pilot tones and thus may adopt a longer cyclic prefix while satisfying the constraint of the overall overhead. In wireless scenarios, pilot tones are needed for fine channel estimation. We may then argue that the same cyclic prefix length and the same number of pilots should be adopted in evaluating both approaches to perform a fair comparison. In this case, since the performance of PTA is determined by the number of pilots, and the performance of CPB depends on $N_g - L + 1$, the results reported in this chapter remains valid as long as $N_g - L + 1 \geq N_p$. When $1 \leq N_g - L + 1 < N_p$ and the frequency offset is nonzero, CPB is worse than PTA at low SNR and is still better than PTA at high SNR, due to CPB's robustness against frequency offset and modulation scheme. The SNR, at which the two performance curves cross each other, increases with the increase of $N_p - (N_g - L + 1)$. Therefore, a hybrid frequency offset tracking structure using both pilots and cyclic prefix is expected to yield better performance and should be further explored.

CHAPTER 6

Optimal Training for OFDM-Based Anytime Anywhere Radio Transmissions

6.1 Introduction

Training is an integral phase of reliable communications over unknown channels. During the training phase, known symbols are transmitted for purposes of channel estimation and synchronization. While too little training results in inaccurate estimates, too much training leaves insufficient time for data transmission before the channel changes. To maintain a maximum throughput for a high data rate wireless mobile system, it is necessary to adapt the amount of training. The knowledge of the optimal training length as a function of channel situations will facilitate the training length scheduling.

For the piece-wise constant approximation of time-varying channels, the optimal training length has been studied in [54]. Under the assumption of perfect synchronization, it is shown from the capacity point of view that at high SNR the optimal training length is equal to the channel length (the minimum meaningful training length); at low SNR, it increases until it converges to a third of the channel coherence interval. However, the assumption of perfect synchronization is not always valid in practical systems, especially when a system employs orthogonal frequency division multiplexing (OFDM) modulation. It is well-known

that OFDM is more sensitive to synchronization errors than to channel estimation errors, due to the longer duration of an OFDM symbol and the inter-carrier interference caused by loss of the carrier orthogonality.

In this chapter we investigate the optimal training length for an OFDM-based system that enables anytime anywhere multimedia transmissions. We approach the problem by deriving the quantitative relationship between training length and system throughput. Effects of both channel estimation error and residual frequency offset are considered. Note that in order to significantly reduce the training overhead, algorithms for blind estimation, synchronization, and detection have been proposed. However, they are only effective when a large amount of data can be collected. This is clearly a disadvantage in the case of mobile wireless communications where the time-varying channel would preclude such data gathering. Also, the high complexity of a blind estimator makes a training-aided estimation the better choice.

The rest of this chapter is organized as follows. Section 6.2 describes the system model used in this study. Section 6.3 analyzes and quantifies the impact of the training length on the system throughput. Section 6.4 derives closed-form expressions of the optimal training length in a variety of scenarios, and verifies the results in simulation. Section 6.5 concludes the chapter.

6.2 System Model

The mobile wireless channel is modelled as a time-varying finite impulse response (FIR) filter with coefficients $h(t, \tau)$, where t is the index of time, and τ is the multipath index. A discrete version of $h(t, \tau)$ can be written as $h(m, l), 1 \leq l \leq L$, where L represents the maximum length of the channel. Let $H(n, k), 1 \leq k \leq K$,

denote the frequency response of the kth tone in the nth OFDM block. Here K is the number of subchannels.

For statistical measures of the channel, channel correlation functions in both the time and frequency domains have been explained in [49]. In this study the coherence bandwidth/time is defined as the bandwidth/time duration over which the frequency/time correlation function is above 0.9. In other words, the coherence bandwidth B_c and delay spread $\Delta\tau$ are linked by

$$B_c = \frac{1}{50\Delta\tau},$$ (6.1)

and the coherence time T_c is related to the Doppler spread f_d by

$$T_c = \frac{1}{f_d}.$$ (6.2)

To simplify our analysis, we further assume that the channel does not change during the transmission of one packet, which can be easily validated through proper packet size scheduling [50, 51].

6.3 Impact of Training Length on Throughput

The system throughput G is calculated by

$$G = \frac{L_p}{L_p + L_t} \cdot R \cdot (1 - P_e)^{L_p}.$$ (6.3)

Here R is the transmission rate which is known and application-dependent, L_p and L_t respectively represent the packet length and training length, and P_e denotes the probability of error. Our goal is to find the optimal L_t which maximizes G. When the packet length is also known, we have a natural constraint on L_t, that is,

$$L \leq L_t \leq L_p.$$

The units of L, L_p, and L_t are samples.

Clearly, the impact of the training length on the system throughput is twofold. On one hand, training overhead reduces the throughput, because less time is spent on data transmission. On the other hand, a long training improves the accuracy of parameter estimation and consequently reduces the probability of error P_e, which to a certain degree compensates the loss in the effective data transmission time. The mathematical description of the first effect is straightforward. However, the mathematical description of the second effect needs clarification of the relationship between L_t and P_e, which obviously is difficult because it involves a variety of parameter estimation tasks.

To simplify our analysis without sacrificing any important term, we consider two dominating estimation errors, i.e., channel estimation error and residual frequency offset. Various methods for estimating the channel frequency /impulse response and frequency offset in OFDM systems have been proposed in the literature [56]-[59, 53]. In this chapter, we assume the use of the best estimators and adopt the corresponding Cramér-Rao bound whenever we address mean square error in estimates. SNR is defined as E_s/N_o.

6.3.1 Effect of Channel Estimation Error

The mean square error in the estimate of the channel frequency response is defined by

$$MSE = E\left\{\frac{1}{K}\sum_{k=1}^{K}\left|\frac{H(n,k) - H(n,k)^{est}}{H(n,k)}\right|^2\right\}, \tag{6.4}$$

where $H(n,k)^{est}$ and $H(n,k)$ represent respectively the estimated and actual subchannel gains. By using the method in [55], the Cramér-Rao lower bound on

the MSE is found to be

$$CRLB = \frac{1}{SNR \cdot L_t}. \tag{6.5}$$

The impact of the MSE on the probability of error P_e depends on the channel modulation scheme. For quadratic amplitude modulation (QAM), it is [52]:

$$P_e^C = 2Q\left[\sqrt{SNR} \cdot \left(1 - \sqrt{2 \cdot MSE}\right)\right], \tag{6.6}$$

where $Q[x] = \int_x^\infty \frac{1}{\sqrt{2\pi}}e^{-y^2/2}dy$. Substituting (6.5) into (6.6), we obtain the expression of the probability of error

$$P_e^C = 2Q\left[\sqrt{SNR} \cdot \left(1 - \sqrt{\frac{2}{SNR \cdot L_t}}\right)\right]. \tag{6.7}$$

Further combining expressions (6.7) and (6.3), we get the direct relationship between the training length and throughput. The numerically obtained optimal training length L_t^* as function of L_p and SNR is depicted in Fig. 6.1. R is set at 50 Kbit/s for facilitating the labelling in figures, and the values of SNR are chosen to yield P_e within the reasonable range of 10^{-5} to 10^{-2}. For a fixed L_p and SNR, we obtain the optimal training length by trying various L_t values within the interval $[2L, L_p]$ and then finding the one that maximizes G. Fig. 6.1 shows the contours of the optimal training length on the plane of (LP, SNR). We observe that at a fixed packet length, the optimal training length L_t^* decreases with the increase of SNR; at fixed SNR, L_t^* increases with L_p. In other words, a longer packet is expected to contribute more time on training. This is not surprising because in order to achieve the same target packet error rate, a longer packet requires lower probability of error which implies the need for a longer training.

Now consider L_t^*/L_p (the ratio of the optimal training length to the packet length). It almost remains constant at fixed SNR, especially for long packets, as shown in Fig. 6.2. Fig. 6.3 demonstrates the corresponding optimal throughput.

Figure 6.1: Contours of optimal training length. Assumption: Channel estimation error dominates.
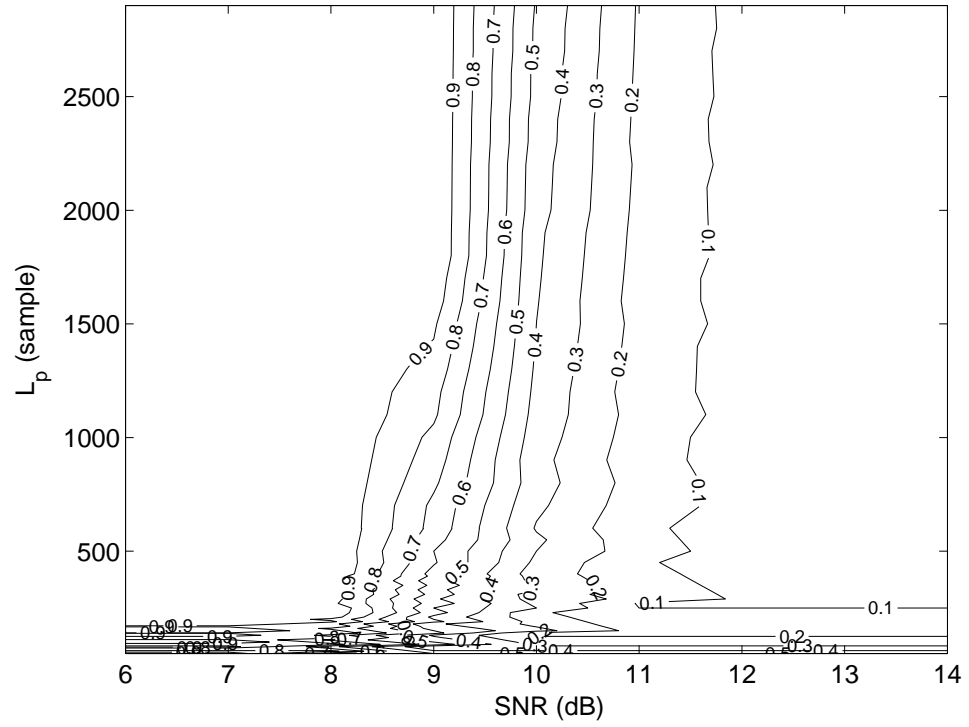
Figure 6.2: Contours of the ratio of optimal training length to packet length. Assumption: Channel estimation error dominates.
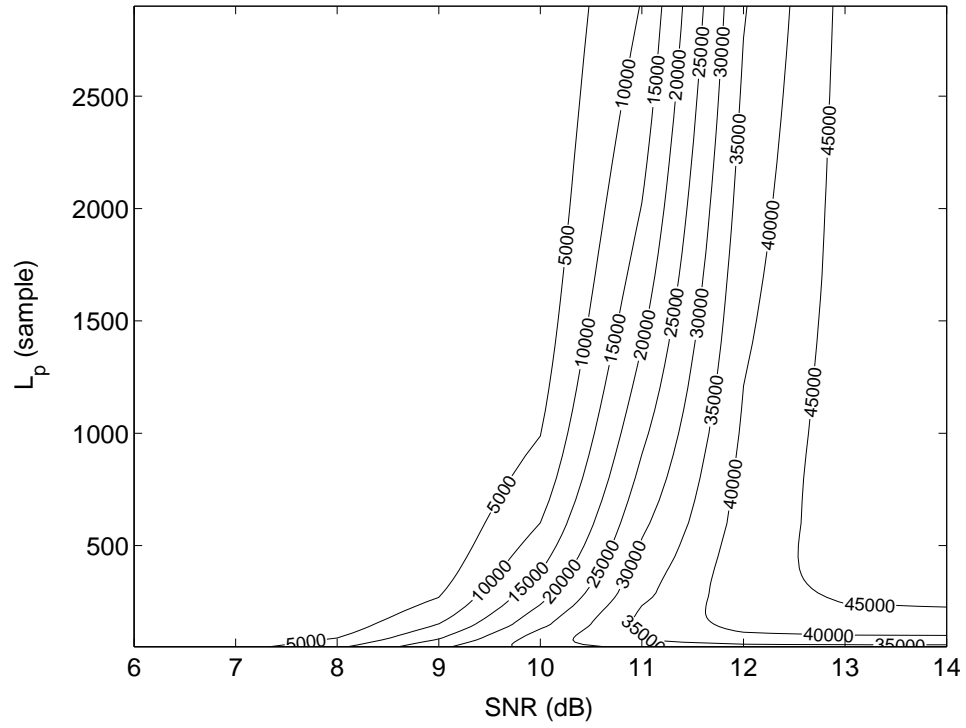
Figure 6.3: Contours of optimal throughput. Assumption: Channel estimation error dominates.

It can be seen that at low SNR (<10 dB), short packets achieve better perfor-
mance than long packets. At moderate SNR (10 dB $\leq$ SNR ≤ 13 dB), short
packets still slightly outperform long packets. However, at high SNR (>13 dB),
a long packet is a better choice.

Note that for time-varying frequency-selective channels, channel mismatch
errors have two origins. One is the inaccurate channel estimation. The other is
the delay in the feedback loop. While error from the first cause can be reduced by
increasing the training length, error from the second cause can only be mitigated
through more frequent channel estimation. The latter is related to packet size
control which has been assumed available in this study.

6.3.2   Effect of Residual Frequency Offset

Now we consider the second dominating estimation error, i.e., residual frequency
offset ϵ. During the training phase, frequency offset Δf between the receiver
and transmitter is estimated by correlating the received counterparts of a pair
of identical sequences of length L_t. The Cramér-Rao lower bound for frequency
offset estimation is [53]

$$CRLB(\Delta f) = \frac{1}{\pi^2 \cdot L_t \cdot SNR}. \tag{6.8}$$

According to the analysis in [44], residual frequency offset ϵ (normalized) results
in SNR degradation in dB of

$$D = \frac{10}{3\ln(10)}\pi^2\epsilon^2 \cdot SNR. \tag{6.9}$$

Assuming ϵ is a variable with zero mean, the average SNR degradation is then

$$E\{D\} = \frac{10}{3\ln(10)}\frac{1}{L_t}, \tag{6.10}$$
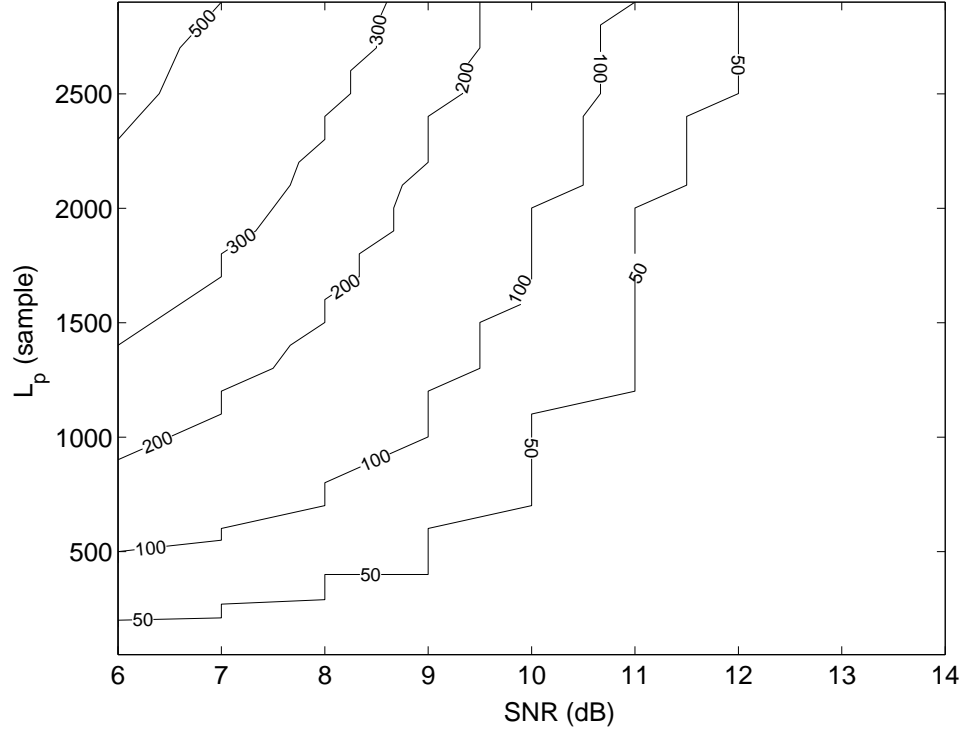
Figure 6.4: Contours of optimal training length. Assumption: Frequency synchronization error dominates.

and the average SNR at the input of the decision device is given by

$$10^{-\frac{1}{3\ln(10)L_t}} \cdot SNR. \tag{6.11}$$

Therefore, the probability of error for QAM is

$$P_e^F = 2Q\left[\sqrt{SNR}\sqrt{10^{-\frac{1}{3\ln(10)L_t}}}\right]. \tag{6.12}$$

Combining expressions (6.3) and (6.12), we obtain L_t^*, L_t^*/L_p, and G^*, and depict them respectively in Figs. 6.4-6.6. We obtain similar observations as those in the previous subsection.
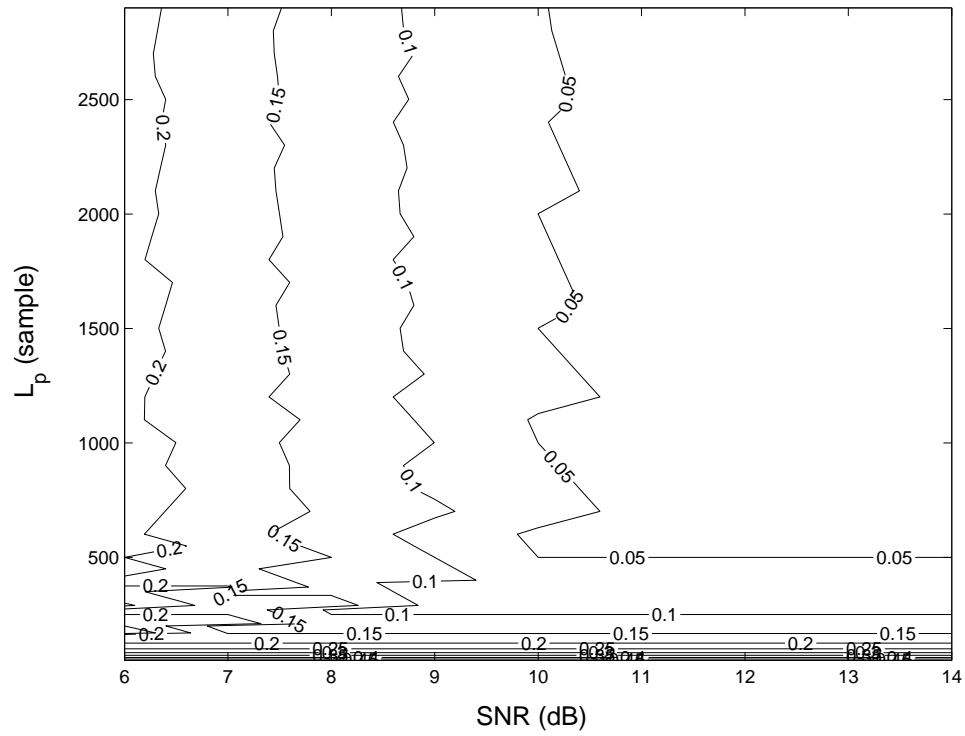
Figure 6.5: Contours of the ratio of optimal training length to packet length. Assumption: Frequency synchronization error dominates.
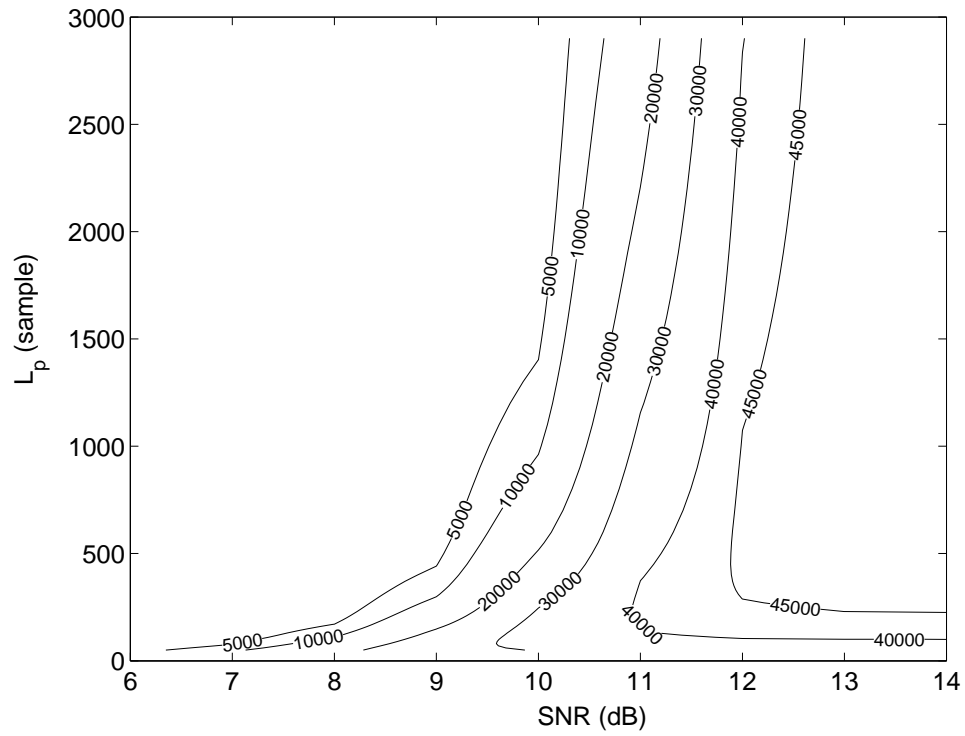
Figure 6.6: Contours of optimal throughput. Assumption: Frequency synchronization error dominates.
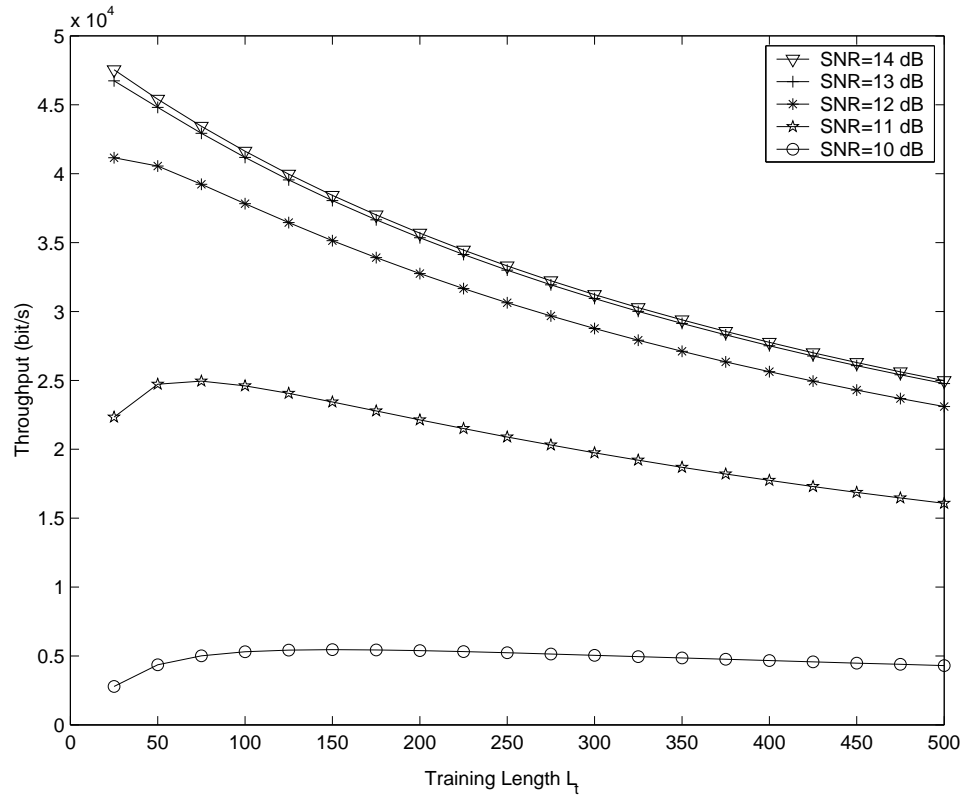
Figure 6.7: Throughput G vs. Training length L_t. Packet length $L_p = 500$ samples.

6.3.3 Combined Effect of Channel Estimation Error and Residual Frequency Offset

Assuming the worst case, the noise terms from the above two error origins are then additive. For QAM, the noise term caused by channel estimation error is $\frac{1}{L_t \cdot SNR}$, and that from residual frequency offset is $\frac{1}{3L_t \cdot SNR}$. Moreover, residual frequency offset reduces the signal power by $\frac{1}{3L_t \cdot SNR}$. Hence, the overall probability of error is

$$P_e = 2Q\left[\sqrt{\frac{1 - \frac{1}{3L_t \cdot SNR}}{\frac{1}{SNR} + \frac{1}{L_t \cdot SNR} + \frac{1}{3L_t \cdot SNR}}}\right] = 2Q\left[\sqrt{\frac{3L_t \cdot SNR - 1}{3L_t + 4}}\right]. \tag{6.13}$$

Clearly the effect of residual frequency offset dominates. This verifies our earlier statement that an OFDM system is usually more sensitive to imperfect frequency synchronization.

6.4 Closed-Form Expressions of the Optimal Training Length

The above numerical results provide helpful information to properly choosing the training length during data transmissions. However, the trial-and-error approach for finding the optimal training length is not feasible in practice. To solve this problem, recall the optimization problem discussed in the previous section:

$$\max_{L \leq L_t \leq L_p} G = \frac{L_p}{L_p + L_t} \cdot R \cdot (1 - P_e)^{L_p}. \tag{6.14}$$

We observe from numerous simulations, that for any fixed L_p and SNR, $G(L_t)$ has a unique global maximum, as illustrated in Fig. 6.7. Therefore, the determination of L_t^* can actually be sought by differentiating G with respect to L_t. In other words, L_t^* is the solution of the following equation

$$\frac{dG}{dL_t} = -\frac{R \cdot L_p}{(L_p + L_t)^2} \cdot (1 - P_e)^{L_p}. \tag{6.15}$$

$$\left[1 + \frac{L_p \cdot (L_p + L_t)}{1 - P_e} \cdot \frac{dP_e}{dL_t}\right] = 0.$$

Assuming P_e is small, which is valid most of the time, we are then able to find the closed-form expressions for the optimal training length.

For channel estimation, differentiating (6.7) with respect to L_t, we get

$$\frac{dP_e^C}{dL_t} = -\frac{1}{\sqrt{\pi}} e^{-\left(\sqrt{SNR} \cdot \left(1 - \sqrt{\frac{2}{SNR \cdot L_t}}\right)\right)^2 / 2} \cdot L_t^{-\frac{3}{2}}. \tag{6.16}$$

Further combine (6.15) and (6.16) to obtain the approximated optimal training length as

$$\hat{L}_t^* = \left(L_p^2 \cdot \frac{1}{\sqrt{\pi}} \cdot e^{-SNR/2}\right)^{\frac{2}{3}}. \tag{6.17}$$

Fig. 6.8 compares L_t^* and $\hat{L}_t^*$. It can be seen that the difference between them is small. Fig. 6.9 further shows that the throughputs resulting from L_t^* and $\hat{L}_t^*$ are in agreement.

For frequency offset estimation, the approximated optimal training length is found to be

$$\hat{L}_t^* = \left(\frac{1}{3\sqrt{2\pi}} \cdot L_p^2 \cdot e^{-SNR/2} \cdot \sqrt{SNR}\right)^{\frac{1}{2}}. \tag{6.18}$$

L_t^* and $\hat{L}_t^*$ are compared in Fig. 6.10. The corresponding system throughput is compared in Fig. 6.11. Again, we observe negligible degradation from using the approximation (6.18).
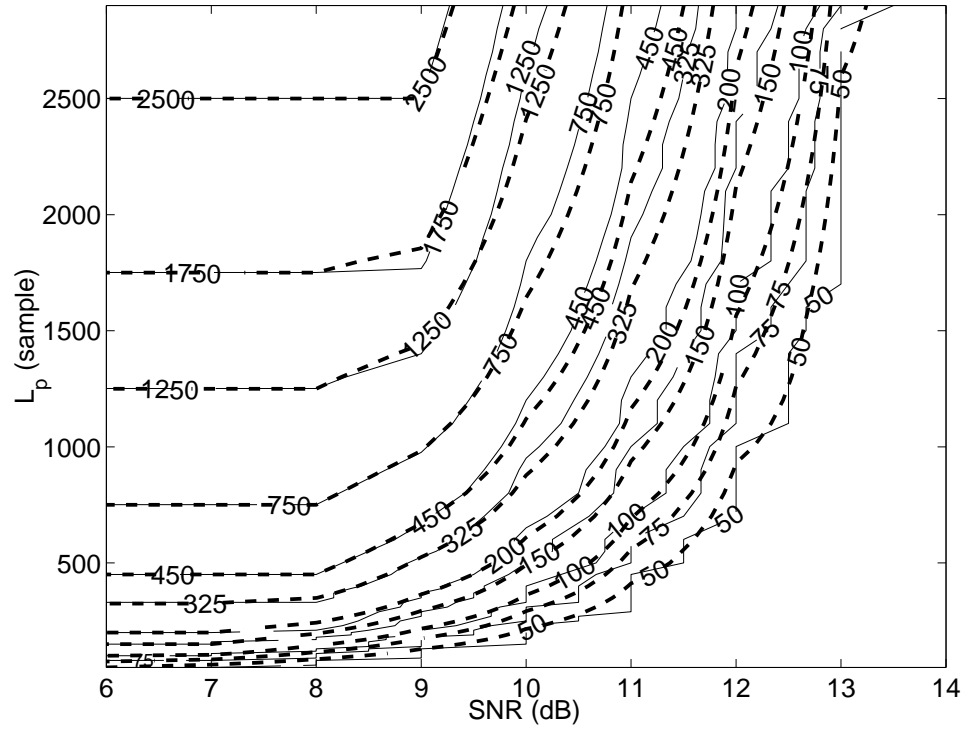
Figure 6.8: Comparison of the actual (solid) and approximated (dashed) optimal training length. Assumption: Channel estimation error dominates.
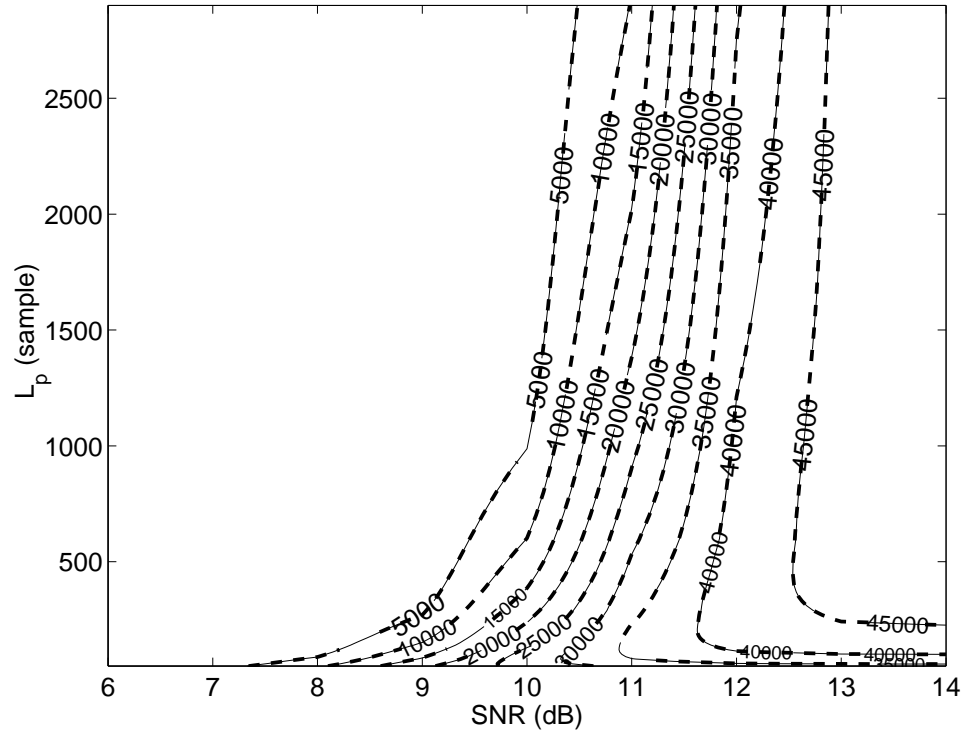
Figure 6.9: Comparison of the actual (solid) and approximated (dashed) optimal throughput. Assumption: Channel estimation error dominates.
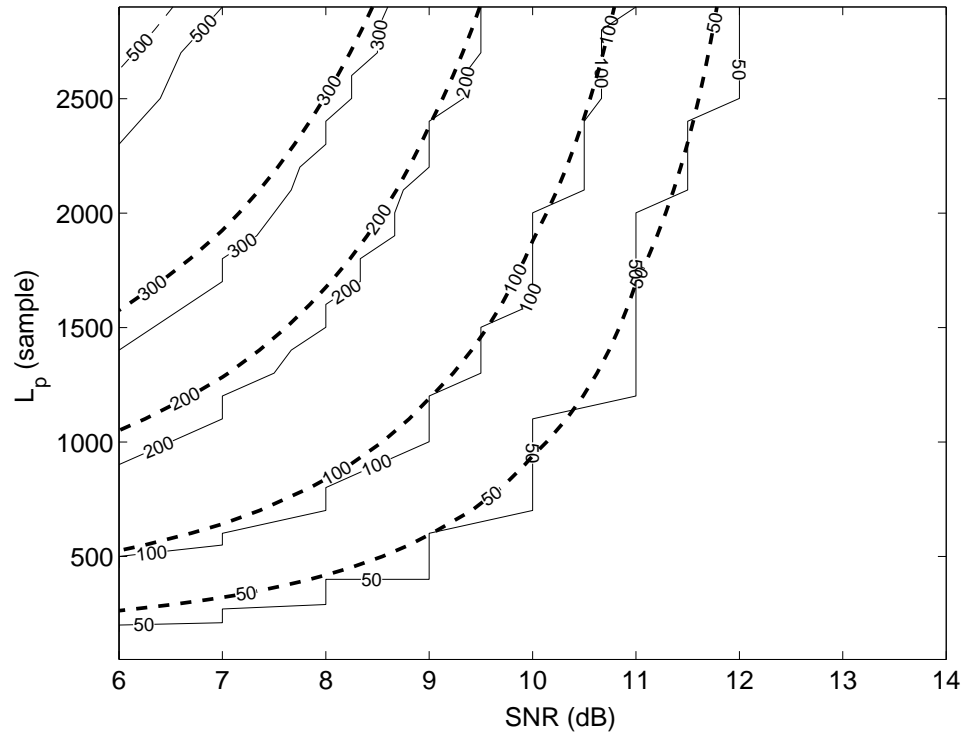
Figure 6.10: Comparison of the actual (solid) and approximated (dashed) optimal training length. Assumption: Frequency synchronization error dominates.
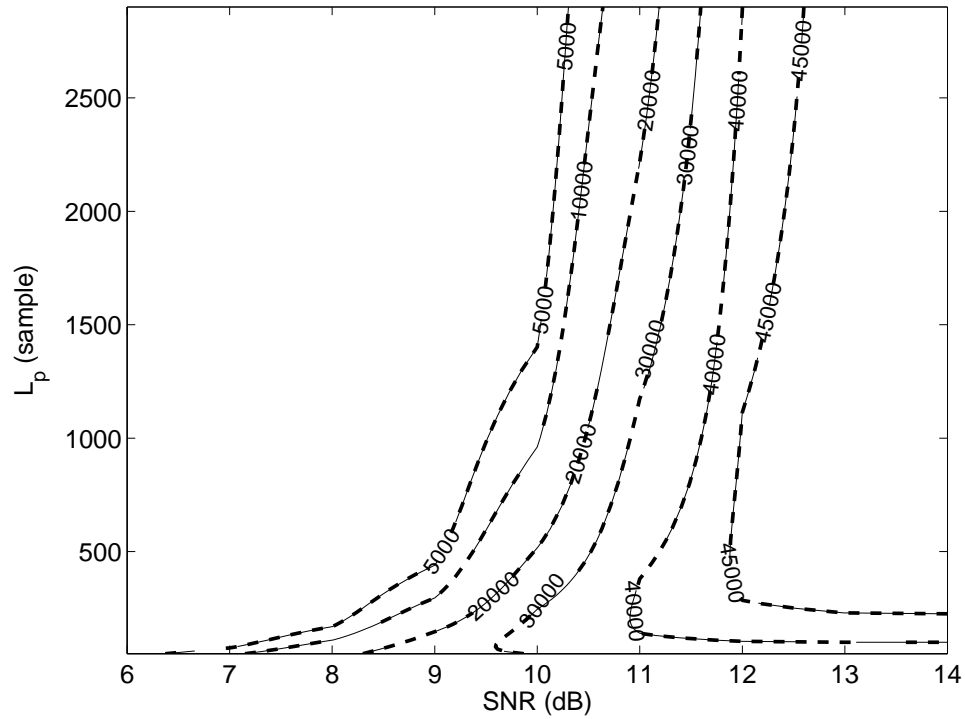
Figure 6.11: Comparison of the actual (solid) and approximated (dashed) optimal throughput. Assumption: Frequency synchronization error dominates.

6.5 Conclusion

We analyzed and quantified the impact of the training length on the system throughput for an OFDM-based wireless communication system. The effects of channel estimation error and residual frequency offset were considered. We illustrated the optimal training length and optimal throughput as function of SNR and packet length. We also obtained closed-form approximations for the optimal training length, which readily lead to low-cost adaptive schemes for practical training length control.

CHAPTER 7

Concluding Remarks and Future Directions

In this study, we addressed several training-related issues for achieving energy-efficient high-speed information transmission over dispersive fiber optic links and radio channels.

We first studied the polarization mode dispersion phenomenon in single-mode fibers. We proposed and validated that a fiber channel with PMD can be characterized as a one-input two-output system. We showed that the system transfer function, described by two finite impulse response (FIR) filters, can be derived from any of the two popularly adopted PMD representations, i.e., a PMD transformation matrix or a PMD vector. Theoretically, an equalization-based PMD compensator can be then readily built based on the knowledge of the two FIR filters. To provide a practical solution, an adaptation scheme is required for adjusting the compensator's coefficients to combat the change of the PMD channel over time. The development of such an adaptive algorithm along with its implementation is not a trivial task and could lead to a new project.

Our effort towards suppressing the PMD effects resulted in a simple training-based scheme that compensates the first-order PMD at low cost.

The present study also contributed to optimizing the performance of an OFDM-based wireless transmission system by discussing and providing insights into the peak-to-average power ratio of OFDM signals, the sensitivity of various

frequency offset tracking methods to key system parameters, and the scheduling of the training sequence length.

We found that the pilot tone-assisted (PTA) algorithm is sensitive to both frequency offset and modulation scheme, and the cyclic prefix-based method (CPB) is sensitive to timing error. Since the PTA scheme also needs greater channel stability (it operates on at least two sequential OFDM blocks), we concluded that CPB is overall a better approach for frequency offset tracking. However, when pilot tones are needed for fine channel estimation, a hybrid frequency offset tracking structure using both pilots and cyclic prefix might be expected to yield better performance. This would be another interesting research project.

Finally, we have shown that the optimal training length is a function of signal-to-noise ratio and packet length, and that the optimal scheduling of the training length can be achieved through transmitter-receiver cooperation. With the increasing demand for multimedia applications, a system design that satisfies Quality-of-Service (QoS) requirements becomes desirable. Hence, cross-layer design, taking into account the bursty nature of wireless data, is emerging as a promising methodology for wireless networks. For example, packet structures may be designed to reflect QoS prioritization. In this case, the optimization of the training length will also be subject to more constraints and become a more challenging research issue.

References

[1] D. R. Goff. A Brief History of Fiber Optic Technology. Fiber Optic Reference Guide, 3rd ed. Focal Press: Woburn, Massachusetts, 2002.

[2] C. D. Poole and J. Nagel. *Optical Fiber Telecommunications*. San Diego, CA: Academic. 114-161, ch. 6, Vol. IIIA, 1997.

[3] H. Kogelnik, R. M. Jopson, and L. E. Nelson. *Optical Fiber Telecommunications*. 725-861, Ch. 15, Vol. IVB, 2002.

[4] J. P. Gordon and H. Kogelnik. PMD fundamentals: Polarization mode dispersion in optical fibers. *PNAS*. 4541-4550, Vol. 97, No. 9, April 2000.

[5] C. D. Poole and R. E. Wagner. Phenomenological approach to polarization dispersion in long single-mode fibers. *Electronics Letters*. 1029-1030, Vol. 22, No. 19, September 1986.

[6] C. D. Poole and C. R. Giles. Polarization-dependent pulse compression and broadening due to polarization dispersion in dispersion-shifted fiber. *Optics Letters*. 155-157, Vol. 13, No. 2, February 1988.

[7] G. J. Foschini and C. D. Poole. Statistical theory of polarization dispersion in single mode fibers. *Journal of Lightwave Technology*. 1439-1456, Vol. 9, No. 11, November 1991.

[8] M. Karlsson. Polarization mode dispersion-induced pulse broadening in optical fibers. *Optics Letters*. 688-690, Vol. 23, No. 9, May 1998.

[9] R. Noé, D. Sandel, M. Yoshida-Dierolf, S. Hinz, V. Mir-voda, A. Schöpflin, C. Glingener, E. Gottwald, C. Scheerer, G. Fisher, T. Weyrauch, and W. Haase. Polarization mode dispersion compensation at 10, 20, and 40Gb/s with various optical equalizers, *J. Lightwave Technology*. 1602-1616, Vol. 17, No. 9, September 1999.

[10] H. Y. Pua, K. Peddanarappagari, B. Zhu, C. Allen, K. Demarest, R. Hui. An adaptive first-order polarization-mode dispersion compensation system aided by polarization scrambling: theory and demonstration. *Journal of Lightwave Technology*, 832-841, Vol. 18, No.6, June 2000.

[11] Q. Yu, L.-S. Yan, Y. Xie, M. Hauer, A. E. Willner. Higher order polarization mode dispersion compensation using a fixed time delay followed by a variable time delay. *IEEE Photonics Technology Letters*. 863-865, Vol. 13, No. 8, August 2001.

[12] J. H. Winters and R. D. Gitlin. Electrical signal processing techniques in long-haul fiber-optic systems, *IEEE Trans. Commun.* 1439-1453, Vol. 38, No. 9, 1990.

[13] H. Bülow, F. Buchali, W. Baumert, R. Ballentin, T. Wehren. PMD mitigation at 10 Gbit/s using linear and nonlinear integrated electronic equaliser circuits. *Electronics Letters*, 163-164, Vol. 36, No. 2, January 2000.

[14] G. J. Foschini, L. E. Nelson, R. M. Jopson, and H. Kogelnik. Probability densities of second-order polarization mode dispersion including polarization dependent chromatic fiber dispersion. *IEEE Photonics Technology Letters.* 293-295, Vol. 12, No. 3, March 2000.

[15] W. Weiershausen, R. Leppla, F. Kuppers, and H. Scholl. Polarization-mode dispersion in fibre transmission: theoretical approach, impact on systems, and suppression of signal-degradation effects. *Proceedings of ECOC'99. 25th European Conference on Optical Communication, Nice, France, 26-30 Sept. 1999.* 130-132, Vol. 2.

[16] T. Merker, N. Hahnenkamp, and P. Meissner. Comparison of PMD-compensation techniques at 10 Gbit/s using an optical first-order compensator and electrical tranversal filter. *Optical Commuincations.* 135-141, August 2000.

[17] C. D. Poole. Dispersion compensation design for lightwave systems. *LEOS '93 Conference Proceedings.* 390-391, 1993.

[18] T. Ono, Y. Yano, L. D. Garrett, J. A. Nagel, M. J. Dickerson, and M. Cvijetic. 10 Gb/s PMD compensation field experiment over 452 km using principal state transmission method. *Proc. Optical Fiber Communication Conference.* PD-44, 2000.

[19] S. Lee, R. Khosravani, J. Peng, V. Grubsky, D. S. Starodubov, A. E. Willner, J. Feinberg. Adjustable compensation of polarization mode dispersion using a high-birefringence nonlinearly chirped fiber Bragg grating. *IEEE Photonics Technology Letters.* 1277-1279, Vol. 11, No. 10, Oct. 1999.

[20] M. Bohn, G. Mohs, C. Scheerer, C. Glingener, C. Wreel, and W. Rosenkranz. An adaptive optical equalizer concept for single channel distortion compensation. *Proceedings of ECOC'01. 27th European Conference on Optical Communication.* 6-7, Vol. 1, 2001.

[21] M.C. Parker, E. Rochat, and S.D. Walker. All-order PMD compensation using filter theory interpretation of Poincaré Sphere trajectories. *Technical Digest.* OFC '02. THGG56. 2002.

[22] H. Chen, C. F. Lam, N. J. Frigo, G. J. Pottie, P. D. Magill, and M. Boroditsky. A One-Input Two-Output Channel Representation for Single-Mode Fibers with PMD. *Journal of Lightwave Technology*. 743-9, Vol. 21, Mar. 2003.

[23] H. Chen, R. M. Jopson, and H. Kogelnik. On the Bandwidth of Higher-Order Polarization-Mode Dispersion: the Taylor Series Expansion. *Optics Express*. 1270-82, Vol. 11, Jun. 2003.

[24] B. W. Hakki. Polarization mode dispersion compensation by phase diversity detection. *IEEE Photonics Technology Letters*. 121-123, Vol. 9, No. 1, Janurary 1997.

[25] F. Buchali, S. Lanne, J.-P. Thiéry, W. Baumert, H. Bülow. Fast eye monitor for 10 Gbit/s and its application for optical PMD compensation. *OFC 2001 Technical Digest*. TuP5-1-3, Vol. 2. March 2001.

[26] Y. Wu and W. Y. Zou. Orthogonal Frequency Division Multiplexing: A Multi-Carrier Modulation Scheme. *IEEE Transactions on Consumer Electronics*. Vol. 41, No. 3, Aug. 1995.

[27] A. N. D'Andrea, V. Lottici, R. Reggiannini. Nonlinear Predistortion of OFDM Signals over Frequency-Selective Fading Channels. *IEEE Transactions on Communications*. pp. 837-843, Vol. 49, No. 5, May 2001.

[28] W. Liu, J. Lau, R. S. Cheng. Considerations on Applying OFDM in a Highly Efficient Power Amplifier. *IEEE Transactions on Circuits and Systems II: Analog and Digital Signal Processing*. pp. 1329-1336, Vol. 46, No. 11, Nov. 1999.

[29] A. Verma and M.T. Arvind. Peak to Average Power Ratio Reduction in Multicarrier Communication Systems. *ICPWC '99*.

[30] J.A. Davis and J. Jedwab. Peak-to-Mean Power Control in OFDM, Golay Complementary Sequences and Reed-Muller Codes. *IEEE Trans. Commun.* Vol. 45, Nov. 1997, pp. 2397-2417.

[31] R. W. Bauml, R. F. H. Fischer, J. B. Huber. Reducing the Peak-to-Average Power Ratio of Multicarrier Modulation by Selected Mapping. *Electronics Letters*. pp. 2056-2057, Vol. 32, No. 22, Oct. 1996.

[32] S.H. Muller and J.B. Huber. OFDM with reduced peak-to-average power ratio by optimum combination of partial transmit sequences. *Electronics Letters*. pp. 368-369, Vol. 33, No. 5, IEE, Feb. 1997.

[33] S.H. Muller and J.B. Huber. A Novel Peak Power Reduction Scheme for OFDM. *IEEE PIMRC'97, Helsinki, Finland.* Sept. 1997.

[34] L.J. Cimini, Jr., and N.R. Sollenberger. Peak-to-Average Power Ratio Reduction of an OFDM Signal Using Partial Transmit Sequences, in *Proc. ICC '99.*

[35] J. Tellado and J. M. Cioffi. Efficient Algorithms for Reducing PAR in Multicarrier Systems. *IEEE International Symposium on Information Theory.* pp.191, Aug. 1998.

[36] B. S. Krongold and D. L. Jones. A New Tone Reservation Method for Complex-Baseband PAR Reduction in OFDM Systems. *ICASSP '02.* pp. (III)2321-2324, Vol. 3, May 2002.

[37] M. Friese. On the Achievable Information Rate with Peak-Power-Limited Orthogonal Frequency-Division Multipexing. *IEEE Transactions on Information Theory.* Vol. 46, No. 7, Nov. 2000.

[38] S.H. Muller and J.B. Huber. A Comparison of Peak Power Reduction Schemes for OFDM. *Proc. IEEE GLOBECOM'97.* pp. 1-5, Vol. 1, Nov. 1997.

[39] X. Li and L.J. Jr. Cimini. Effects of Clipping and Filtering on the Performance of OFDM. *IEEE Communications Letters.* pp. 131-133, Vol, 2, No. 5, May 1998.

[40] S. B. Slimane. Peak-to-Average Power Ratio Reduction of OFDM Signals using Broadband Pulse Shaping. *IEEE 56th Vehicular Technology Conference.* pp. 889-893, Vol. 2, Sept. 2002.

[41] L. J. Cimini. Analysis and Simulation of a Digital Mobile Channel using Orthogonal Frequency Division Multiplexing. *IEEE Transactions on Communications.* pp. 665-675, Jul. 1985.

[42] Framing Structure, Channel Coding and Modulation for Digital Terrestrial Television, EN 300 744 V 1.1.2, 1997.

[43] HIPERLAN Type 2, Physical (PHY) Layer, ETSI TS 101 475 V 1.2.1A, 2000.

[44] T. Pollet, M. Van Bladel, and M. Moeneclaey. BER Sensitivity of OFDM Systems to Carrier Frequency Offset and Wiener Phase Noise. *IEEE Transactions on Communications.* pp. 191-193, Vol. 43, No. 2, Feb. 1995.

[45] M. Morelli and U. Mengali. An Improved Frequency Offset Estimator for OFDM Applications. *IEEE Communications Letters.* pp. 75-77, Vol. 3, No. 3, Mar. 1999.

[46] T. Keller, L. Piazzo, P. Mandarini, and L. Hanzo. Orthogonal Frequency Division Multiplex Synchronization Techniques for Frequency-Seclective Fading Channels. *IEEE Journal on Selected Areas in Communications.* pp. 999-1008, Vol. 19, No. 6, Jun. 2001.

[47] N. Lashkarian and S. Kiaei. Class of Cyclic-Based Estimators for Frequency-Offset Estimation of OFDM Systems. *IEEE Transactions on Communications.* pp. 2139-2149, Vol. 48, No.4 12, Dec. 2000.

[48] http://grouper.ieee.org/groups/802/15/arc/802-wpanlist/ msg00305.html

[49] T. S. Rappaport. Wireless Communications: Principles and Practice (2nd Edition).

[50] E. Modiano. An Adaptive Algorithm for Optimizing the Packet Size Used in Wireless ARQ Protocols. *Wireless Networks.* pp. 279-286, Vol. 5, 1999.

[51] P. Lettieri and M. B. Srivastava. Adaptive Frame Length Control for Improving Wireless Link Throughput, Range, and Energy Efficiency. *INFOCOM '98.* pp. 564-571, Vol. 2, 29 Mar-2 Apr 1998.

[52] A. Leke and J.M. Cioffi. Impact of Imperfect Channel Knowledge on the Performance of Multicarrier Systems. *Global Telecommunications Conference, 1998.* pp. 951-955, Vol. 2, 1998.

[53] T. M. Schmidl and D. C. Cox. Robust Frequency and Timing Synchronization for OFDM. *IEEE Transactions on Communications.* pp. 1613-1621, Vol. 45, No. 12, Dec. 1997.

[54] H. Vikalo, B. Hassibi, B. Hochwald, and T. Kailath. Optimal Training for Frequency-Selective Fading Channels. *IEEE International Conference on Acoustics, Speech, and Signal.* pp. 2105-2108, Vol. 4, 2001.

[55] N. S. Alagha. Cramer-Rao bounds of SNR estimates for BPSK and QPSK Modulated Signals. *IEEE Communications Letters*, pp. 10-12, Vol. 5, No. 1, Jan. 2001.

[56] O. Edfors, M. Sandell, J.-J. van de Beek, S. K. Wilson, P. O. Borjesson. OFDM Channel Estimation by Singular Value Decomposition. *IEEE Transactions on Communications.* pp. 931-939, Vol. 46, No. 7, July 1998.

[57] Y. Li, L. J. Jr. Cimini, N. R. Sollenberger. Robust Channel Estimation for OFDM Systems with Rapid Dispersive Fading Channels. *IEEE Transactions on Communications*. pp. 902-915, Vol. 46, No. 7, July 1998.

[58] P. H. Moose. A Technique for Orthogonal Frequency Division Multiplexing Frequency Offset Correction. *IEEE Transactions on Communications*. pp. 2908 -2914, Vol. 42, No. 10, Oct. 1994.

[59] F. Classen and H. Meyr. Frequency Synchronization Algorithms for OFDM Systems Suitable for Communication over Frequency Selective Fading Channels. *IEEE 44th Vehicular Technology Conference*. pp. 1655-1659, Vol.3, Jun. 1994.

[60] L. Tong, A. Swami, A. Ephremides, D. Goeckel, A. Scaglione, and S. Servetto. Future Challenges of Signal Processing and Communications in Wireless Networks. *NSF/ONR/ARL Workshop*, 2002.